Assessing the consistency of eddy covariance measurements under conditions of sloping topography within a hilly agricultural catchment

Rim Zitouna, Laurent Prevot, Frédéric Jacob, Raoudha Mougou, Marc Voltz

Assessing the consistency of eddy covariance measurements under conditions of sloping topography within a hilly agricultural catchment.

Rim Zitouna-Chebbi [a,*], Laurent Prévot [b], Frédéric Jacob [c], Raoudha Mougou [a], Marc Voltz [b]

a INRGREF, LR GERE, Tunis, Tunisia
b INRA, UMR LISAH, Montpellier, France
c IRD, UMR LISAH, Montpellier, France

*Corresponding author:

Rim Zitouna-Chebbi
Institut National de Recherches en Génie Rural, Eaux et Forêts
Laboratoire de Recherche « Gestion des Risques Environnementaux en Agriculture »
Rue Hédy Karray
BP 10, Ariana 2080
Tunisie
Tel: +216-71-709-033
Fax: +216-71-717-951
rim.zitouna@iresa.agrinet.tn, rimzitouna@live.fr

***Highlights (for review)**

- Eddy covariance (EC) measurements over hillslope under forced convection
- Upward flows: agreement between topography and EC derived airflow inclinations
- Downward flows: differences between topography and EC derived airflow inclinations
- Downward flows: differences ascribed to separation bubble with streamline dilatation
- Energy balance closure similar to reports on flat and mountainous topographies

ABSTRACT

The current study addressed the consistency of Eddy Covariance (EC) measurements collected in sloping conditions within a hilly agricultural catchment. In the context of operational monitoring and modelling devoted to decision support, it is important to increase the knowledge of surface fluxes under conditions of hilly topography. The two-metre-high EC measurements were collected at the field scale within the two opposite rims of a V-shaped catchment located in northeastern Tunisia on the southern shore of the Mediterranean Basin. Measurements were collected under bare soil conditions to enhance the effects of the slopes. The data pre-processing and quality control measures were conducted using standard procedures. In assessing the consistency of the EC measurements we first compared the airflow inclinations captured by the EC measurements against the topographical slopes captured by a Digital Elevation Model; we then assessed the energy balance closure. The analysis of the micrometeorological data indicated specific regimes: externally driven winds; forced convection; and stability conditions close to neutrality or low instability. The two dominant wind directions induced upward and downward flows on the two opposite rims. For the upward flows, the airflow inclinations followed the topographical slopes on both fields. For the downward flows, the flows followed the topographical slopes on the southern rim and were almost horizontal on the other rim. In all cases, and especially for the upward flows, the energy balance closure was similar to that reported in the literature. Overall, the behaviour observed for upward flows was close to that reported in the literature for flat conditions, whereas the downward flows exhibited different trends. The different trends we observed for the downward flows were ascribed to the bubble separation zone that implies streamline dilatation, turbulence and reverse flows. Future investigations should address the vegetation conditions. The expected outcomes are of importance for revisiting the operational methods devoted to the estimation of evapotranspiration.

KEYWORDS: agricultural hilly catchment, eddy-covariance measurements, sloping conditions, airflow inclination, land surface energy balance.

1. INTRODUCTION

Knowledge of land surface energy fluxes is of paramount importance for water and crop management within semi-arid regions, where the annual actual evapotranspiration amounts to more than two-thirds of the yearly precipitation (Moussa et al., 2007; Daneshkar Arasteh and Tajrishy, 2008). Numerous methods have been developed for measuring and modelling the land surface energy fluxes in flat terrain (Rana and Katerji, 2000; Olioso et al., 2002a; Courault et al., 2005). However, little research has been performed for the hilly catchments that correspond to large agricultural areas in many regions of the world (e.g., Mediterranean countries, western Africa, eastern India). Hilly catchments allow water harvesting to be used to secure agricultural production (Mekki et al., 2006; Saha et al., 2007). Our understanding of the energy fluxes and crop evapotranspiration within hilly catchments is still incomplete; a major gap in the knowledge is the influence of the topography on the structure of turbulence within the boundary layer (Raupach and Finnigan, 1997).

Understanding the airflows and surface fluxes over hills was first investigated with wind tunnels (Jackson and Hunt, 1975; Brunet et al., 1994; Poggi and Katul, 2007), and analytical solutions have been proposed for wind and temperature profiles (Jackson and Hunt, 1975; Hunt et al., 1988; Raupach et al., 1992; Kaimal and Finnigan, 1994; Finnigan and Belcher, 2004). However, applying these formulations over hilly catchments is questionable because they are limited to simple two-dimensional hills. Another possibility is the large eddy simulation (LES) technique (Tamura et al., 2007; Dupont et al., 2008). However, LES implementation is a delicate task that requires substantial computer resources, especially over the heterogeneous landscapes that involve large spatial extents and fine spatial resolutions. Furthermore, the application of LES is still limited to simple topography (Dupont et al., 2008).

As a result of the aforementioned modelling difficulties and of the increasing availability of eddy covariance (EC) systems, several experimental campaigns have investigated the effects of sloping conditions. These campaigns have involved single flux towers either under mountainous conditions with forests (Geissbühler et al., 2000; Humphreys et al., 2003; Turnipseed et al., 2003) and grasslands (Hammerle et al., 2007; Hiller et al.,

2008), or within hilly catchments with crop systems (Rana et al. 2007; Scott, 2010). Until recently, the experimental costs made it almost impractical to analyse turbulence and advection from the data collected by several nearby EC systems (Feigenwinter et al., 2008).

The effects of slope have been taken into account by applying rotational corrections to the EC measurements, such as the latter fitted to the airflow planes induced by the topographical slopes. When dealing with the single EC towers within hilly agricultural catchments, the energy flux data corrected for slope effects were next used to address the modelling of turbulent exchanges. Thus, Rana et al. (2007) proposed a semi-empirical correction to the turbulent exchange coefficients that accounts for the slope magnitude by extending to non-neutral conditions the neutral wind speed profile relationship proposed by Kaimal and Finnigan (1994). However, follow-up research is needed to extend the few existing works on the EC measurements from single towers; to enable such measurements to be used operationally for monitoring water consumption by crops in hilly catchments, especially in semi-arid regions.

The objective of the current study was to increase the understanding of EC measurements from single towers in sloping conditions within hilly agricultural catchments; by investigating the possible links between the topography, airflow inclinations driven by the wind direction, and surface energy balance closure. We considered a Mediterranean agricultural catchment with hilly topography, locating the EC measurements on the two opposite sides of a valley. We addressed bare soil conditions only, to minimise land-use heterogeneity effects and thus enhance the effects of topography. Section 2 presents the study area, the data collection and processing, including the flux calculation, quality control and footprint analysis, and topographical characterisation from a digital elevation model (DEM). Section 3 reports the analysis of micrometeorological conditions (wind regimes and stability conditions), as well as the results obtained when comparing the airflow inclinations against the topographical slopes and when verifying the energy balance closure according to the airflow inclinations. Section 4 discusses the main outcomes and future directions.

2. MATERIALS AND METHODS

2.1 Experimental site and calendar

The experiment was set within the agricultural Kamech catchment, which is located in the Cap Bon Peninsula in northeastern Tunisia (36°52'40"N, 10°52'40"E, Fig. 1). Comprehensive descriptions of the Kamech catchment are given by Mekki et al. (2006) and Raclot and Albergel (2006). This catchment belongs to the long-term environmental research observatory OMERE (a French acronym for the Mediterranean Observatory of Water and the Rural Environment). Within Mediterranean rural catchments, the OMERE studies the impacts of anthropogenic forcing and climate change on hydrology, erosion, and water quality in relation to pollutants (http://www.umr-lisah.fr/omere).

[Figure 1 about here]

The 2.45 km² Kamech catchment is crossed by the El Gameh wadi from the northeast to the southwest (Fig. 2). The catchment topography is entirely V-shaped from the middle to the south-western parts. The slopes are irregular, especially on the southern rim, which has natural embankments induced by sandstone hogbacks. The altitude ranges between 94 m and 194 m. The slopes range between 0% and 30%, the quartiles being 6%, 11% and 18%. Most fields have a small size with an average area of 0.6 ha. The soils have sandy-loam textures, with depths ranging from zero to two metres according to the location within the catchment and the local topography. These swelling soils exhibit shrinkage cracks under dry conditions during the summer (Raclot and Albergel, 2006). The main crops are winter cereals and legumes. The steepest parts of the catchment are used as rangeland for livestock and are therefore covered by natural vegetation. The regional climate is sub-humid with annual values of 600 mm and 1500 mm for the precipitation and Penman-Monteith reference crop evapotranspiration, respectively. Because of the combination of sub-humid climate and rain-fed agriculture, the catchment is under bare soil conditions from the end of spring to the middle of autumn.

[Figure 2 about here]

The flux measurements were conducted under bare soil conditions during several months in 2004 and 2006. For both years, a flux station was installed in Field A, located on the northern rim of the catchment (Fig. 2). Field A had an area of 1.1 ha with an homogeneous slope of 5° facing the south-southeast direction (Fig. 2 and Fig. 3). This field's northern (and upper) limit was close to the rim top, which forms the catchment edge. To collect data on the opposite rim and subsequently to assess the possible effect of slope orientation on energy fluxes, a second flux station was installed in 2006 in Field C, located on the southern rim of the catchment (Fig. 2) and facing northwest. Field C had an area of 2.2 ha and a rugged topography (Fig. 3). The averaged slope around the field centre was approximately 8°. The southern (and upper) limit was close to a plateau, located in the middle of the rim. The northern limit had a natural embankment induced by a sandstone hogback.

[Figure 3 about here]

Concentrating on bare soil conditions allowed (1) the removal of vegetation canopy effects, which had an influence on the turbulent fluxes that could be as strong as that of topography (Turnipseed et al., 2003), and (2) a focus on periods during which the land surface conditions were homogeneous throughout the catchment. In 2004, the measurements were collected in Field A from 18 July to 4 November. In 2006, the measurements were collected on fields A and C from 20 June to 28 July. The corresponding three data sets were labelled A04, A06 and C06, where the letter represents the field, and the two digits represent the year.

2.2. Instrumentation and data acquisition

A meteorological station located near the catchment outlet (labelled M on Fig. 2) measured: (1) the rainfall at a daily time step with a manual raingauge; (2) the solar irradiance with a SP1110 pyranometer (Skye, UK); (3) the air temperature and humidity with an HMP45C probe (Vaisala, Finland); (4) the wind speed with an A100R anemometer (Vector Instruments, UK); and (5) the wind direction with a W200P wind vane (Vector Instruments, UK). The instruments were installed 2 m above ground (except the raingauge, which was set up at 1 m) and were connected to a CR10X data-logger (Campbell Scientific, USA).

Variables were samples at 1 Hz and stored as 30-minute averages. All of the instruments were either new or recently new and had been calibrated by the manufacturer.

The sensible and latent heat fluxes, soil heat flux and net radiation were measured with similar flux stations at fields A and C. The instruments for each flux station are listed in Table 1. Because the CR23X data-logger has a limited storage capacity, the raw sonic anemometer and krypton hygrometer data were collected at a 10 Hz frequency and stored on the LoggerNet final storage area #2 of the CR23X data-logger. These raw data were then downloaded every minute to a laptop through the RS232 serial port. The instruments on Field A in 2004 and on Field C in 2006 were three months old. On field A in 2006, the two-year-old krypton hygrometer did not operate.

[Table 1 about here]

The three soil heat flux sensors were distributed two metres away from the station, and were buried between 20 and 50 mm below the soil surface. The net radiometers were installed 1.5 m above the ground. The sonic anemometers, the krypton hygrometers, and the air temperature and humidity probes were installed at the same height above the ground during each period of data acquisition: 1.96 m for Field A in 2004 (data set A04); 1.78 m for Field A in 2006 (dataset A06); and 2.02 m for Field C in 2006 (data set C06). The sonic anemometer verticality and the net radiometer horizontality were carefully checked during the experiments with spirit levels, but no realignment needed to be performed. The accuracy of the double spirit level used for the Young sonic anemometer was 0.5 mm/m, corresponding to an angle of 0.03°. Accuracy on the integrated spirit level of the CSAT sonic anemometer was unknown. Overall, we assumed the accuracy on device alignment was better than 1°. This proposed accuracy was further indirectly confirmed when comparing the flow inclination captured in 2004 and 2006 by the EC device on the same location within Field A. Indeed, the differences between both years were less than 2° (Section 3.3.2) (Fig. 8a and 8b).

The alternation between the dry and wet periods degraded the krypton hygrometer KH20. As a result, the KH20 did not operate in 2006 at Field A, and no latent heat flux data were collected for the data set A06. The data acquisition systems were powered by batteries

214 and solar panels. Because of the high power consumption of the laptop computers, several
215 battery failures occurred, and the 10 Hz data acquisitions were not continuous. Furthermore,
216 only daytime data were considered for analysis in the context of quantifying
217 evapotranspiration. The daytime periods were defined by the 30-minute intervals during
218 which the positive values of solar irradiance were measured. After gap removal and daytime
219 observation selection, the numbers of 30-minute intervals with 10 Hz data acquisition were
220 375, 463 and 579 for data sets A04, A06 and C06, corresponding to 10%, 25% and 30% of
221 the experiment durations, respectively.
222
223 **2.3 Calculation of net radiation and soil heat flux**
224
225 A side-by-side comparison of NR-lite net radiometer measurements was conducted
226 during one month over a natural grass field. This comparison was aimed at ensuring that both
227 the measurements and the subsequent behaviour on the two opposite rims of the V-shaped
228 catchment could be cross-analysed. The comparison of the net radiation data indicated a root
229 mean square difference of 20 W m^{-2} (5% relative). This difference was notably close to the
230 instrument accuracies. Thus, no correction was applied.
231
232 Measurements of net radiation (Rn) were corrected for the effects of slope following
233 the procedure proposed by Holst et al. (2005). Only the direct solar irradiance was corrected
234 by accounting for the angle between the solar direction and the normal to the local
235 topography. The solar direction was derived from time, latitude and longitude with
236 astronomical rules. The local topography was characterised by the slope (topographical zenith
237 with nadir as origin) and aspect (topographical azimuth with north as origin). Both the slope
238 and aspect were calculated using a four-metre spatial resolution DEM obtained by
239 photogrammetry from a stereo pair of panchromatic Ikonos images (Raclot and Albergel,
240 2006). The direct solar irradiance was derived from total solar irradiance measured at the
241 meteorological station (Section 2.2). For this, the diffuse solar irradiance was expressed as an
242 empirical function of atmospheric transmittance; the latter was estimated as the ratio of the
243 solar irradiance measured at the meteorological station to the extra-terrestrial solar irradiance
244 derived from the astronomical rules. The empirical function was calibrated beforehand over
245 the ReSeDA meteorological database that is representative of typical Mediterranean climates

(Olioso et al., 2002b). The obtained calibration was notably close to that proposed by Collares-Pereira and Rabl (1979) and used by Holst et al. (2005).

The average correction of the net radiation measurements for slope effects was approximately 40 W m^{-2} (12% relative) and 55 W m^{-2} (15% relative) for fields A and C, respectively, as indicated by the root mean square differences between corrected and non-corrected data. The maximum corrections reached 60 W m^{-2} for Field A and 100 W m^{-2} for Field C, and they corresponded to the sunrise or sunset. On average, the corrections induced an increase (respectively decrease) of net radiation measurements on Field A (respectively C). Such between-field differences can be explained by field aspects, because Field A (respectively C) faced the south-southeast (respectively northwest) direction (Section 2.1).

The measurements of soil heat flux (G) are usually corrected for the heat storage between the surface and the sensors (Heusinkveld et al., 2004; Liebethal et al., 2005). However, no correction was performed here because the existing solutions are questionable when considering swelling soils that exhibit shrinkage cracks under dry conditions during the summer (Section 2.1). Neglecting the heat storage induced errors in the soil heat flux measurements of between 20 and 50 W m^{-2} (20% to 50% relative), as reviewed by Foken (2008). It was a posteriori verified when analysing the energy balance closure that such errors in soil heat flux were not critical (Section 3.4). Finally, soil heat flux was estimated as the mean value of the measurements collected by the three soil heat sensors distributed around each of the two stations.

2.4 Calculation of the EC-based convective fluxes and airflow inclinations

The three convective fluxes (friction velocity u_*, sensible heat flux H and latent heat flux λE) and the angles for characterising the airflow inclinations were calculated from the 10 Hz data collected with the sonic anemometer and the krypton hygrometer with the ECPACK library version 2.5.22 (http://www.met.wau.nl/projects/jep/report/ecromp/, van Dijk et al., 2004). We present hereafter the different steps of the calculations. We note u_* was used for both controlling the data quality and calculating the EC data footprint.

278 2.4.1 Instrumental corrections

279

280 The entire set of instrument corrections proposed in the aforementioned version of the
281 ECPACK library was applied. These corrections addressed the following items: (1) the
282 calibration drift of the krypton hygrometer with the air humidity and temperature measured by
283 the HMP45C probe over each 30-minute interval; (2) the linear trends over the 30-minute
284 intervals; (3) the sonic anemometer temperature for humidity; (4) the hygrometer response for
285 oxygen sensitivity; (5) the mean vertical velocity (Webb term); and (6) the correction for the
286 frequency response (spectral loss) and path averaging. In relation to a low measurement
287 height of approximately 2 m above surface level (Section 2.2), the correction for the
288 frequency response increased the flux magnitudes by 0.01 m s^{-1} (2% relative), 10 W m^{-2} (5%
289 relative) and 5 W m^{-2} (8% relative) for u_*, H and λE, respectively. The resulting convective
290 fluxes were labelled NR for Non-Rotated.

291

292 A side-by-side comparison of the EC device measurements was conducted during one
293 month within Field A. This comparison aimed at ensuring it was possible to compare the
294 measurements and subsequent behaviour on the two opposite rims of the V-shaped catchment.
295 The comparison of convective flux data indicated a root mean square difference of 20 W m^{-2}
296 (15% relative). This difference was close to the accuracy of the EC data, which are widely
297 accepted to be between 20 and 50 W m^{-2} for the latent heat and between 10 and 30 W m^{-2} for
298 the sensible heat flux, which corresponds to 5–20% relative (Foken, 2008). Thus, no
299 correction was applied.

300

301 2.4.2 Rotational corrections and airflow inclination

302

303 The sonic anemometers were installed vertically, although the sloping conditions were
304 suspected to induce non-horizontal airflows. The rotational corrections were applied to correct
305 the fluxes for the airflow inclination, as explained hereafter.

306

307 The three-dimensional sonic anemometers measure wind speed in three perpendicular
308 directions (labelled u and v in the horizontal plane and w in the vertical). When estimating the
309 convective fluxes from the EC measurements, the rotations are usually applied to the

coordinate system (Kaimal and Finnigan, 1994). Over flat terrain, the aim is to account for the incorrect vertical alignment of the sonic anemometer. Over slopes, the aim is to virtually align the sonic anemometer perpendicularly to the airflow streamlines (Geissbühler et al., 2000; Humphreys et al., 2003; Lewicki et al., 2008). These rotations are usually defined by three angles: the yaw angle, which is a rotation around the vertical axis that aligns u with the wind direction; the pitch angle, which is a rotation around the horizontal axis perpendicular to the wind direction that sets w to zero; and the roll angle, which is a rotation around the horizontal axis parallel to the wind direction.

Amongst the existing possibilities for performing rotational corrections, we selected the planar fit correction introduced by Wilczak et al. (2001) and implemented in the ECPACK library. This method has been recommended by several authors (Massman and Lee, 2002; Turnipseed et al., 2003; Lee et al., 2004) for correcting EC measurements acquired over sloping terrain. Assuming the airflow streamlines are included in a plane, the latter is fitted to a set of wind speed components collected over a long time interval, typically ranging from one to several days. Thus, the planar fit correction is less sensitive to the sampling errors than the double and triple rotation corrections (Turnipseed et al., 2003), where the latter are applied to each integration interval (30 minutes in our case). Because the current study focused on the daytime data, the planar fit correction did not suffer from uncertainties resulting from low night-time wind speeds.

Over heterogeneous terrain that induces anisotropic airflow, the tilt angles (pitch and roll) are likely to depend upon the wind direction (yaw angle). Consequently, the airflow inclination for various wind directions cannot be adequately represented by a single plane only. The 10-Hz EC data were therefore grouped according to wind direction (or wind sectors). Two calculations were made to ensure that the planar fit angles were not sensitive to the time interval over which they were estimated. A single plane was fitted over all of the data belonging to a wind sector for a given data set (A04, A06, and C06). Additionally, for a given field (A or C), one plane was fitted for each wind sector and each day. We a posteriori verified that considering these two methods provided similar results for airflow inclination, as captured with planar fit angles (Section 3.3) and flux magnitude (Section 3.4).

342 The planar fit provided the inclination angles of the plane that fitted the wind speed
343 components over a given time interval in which the angles are in a coordinate system fixed to
344 the anemometer. For a given plane inclination provided by the planar fit angles, along with
345 the anemometer orientation that had previously been determined when setting up each flux
346 station, it was possible to calculate the airflow inclination for any wind direction, including
347 those that corresponded to the yaw angle measurements.
348
349 Finally, the planar fit angles calculated at the daily timescale for each wind sector were
350 introduced into the planar fit correction of the fluxes, and the resulting convective fluxes
351 calculated over 30-minute intervals were labelled PF (Planar Fit).
352
353 2.4.3 Quality control
354
355 The quality control of the 30-minute flux data was performed using two standard tests
356 that are routinely employed over sloping terrains. These tests ensure that the theoretical
357 requirements for the EC measurements are fulfilled (Geissbühler et al., 2000; Rebmann et al.,
358 2005; Hammerle et al., 2007, Hiller et al., 2008).
359
360 The steady-state (ST) test (Foken and Wichura, 1996) characterises the turbulence
361 time homogeneity for the three convective fluxes. This test compares the average flux values
362 over each 30-minute interval with the averaged values over the six corresponding 5-minute
363 subintervals. The integral turbulence characteristics (ITC) test (Foken and Wichura, 1996;
364 Rebmann et al., 2005) characterises the development of turbulence and therefore the spatial
365 homogeneity in terms of the surface aerodynamic properties. For that characterisation, the test
366 compares the measured flux-variance similarities to those obtained from the empirical models
367 based on Monin-Obukhov similarity theory. Over each 30-minute interval, the flux-variance
368 similarities are tested for the horizontal wind speed u, vertical wind speed w and air
369 temperature T.
370
371 Both the ST and the ITC tests are expressed as absolute values of the relative
372 differences. These tests allow the data to be ranked (Foken et al., 2004; Rebmann et al.,
373 2005): the high-quality turbulence data (test values less than 0.3); good quality data for the

flux measurements (test values between 0.3 and 1.0); and low-quality data (test values greater than 1.0).

2.4.4 Footprint of the EC fluxes

Quantifying the area that contributed to each flux measurement – the so-called footprint area – was an important step for characterising the representativeness of the measured fluxes. This step was also important for analysing any topographical influence on the flux measurements because this analysis required the knowledge of the relief within the contributing areas.

The footprint of each 30-minute sample of the EC flux data was estimated using the approach of Horst and Weil (1994), which relies on an analytical dispersion model that accounts for the effects of atmospheric stability. The Horst and Weil model offered a good compromise between ease of implementation and estimate reliability. Furthermore, the assumption of the spatial uniformity and temporal constancy of the surface roughness in the Horst and Weil model was well-fulfilled during the experiment because (1) each field and all surrounding plots were bare soil only, and (2) the flux data were filtered using the ST and ITC tests (see Section 2.4.3). For each flux estimate derived from the EC data via the ECPACK library, the footprint area was calculated from the outputs of the Horst and Weil model as the ellipsoid from which 90% of the flux originated. Each footprint ellipsoid was characterised by its length (respectively width) along (respectively across) the wind direction. The footprint ellipsoids were then combined with the digital map of the field boundaries (Fig. 3) to quantify the proportion of the measured fluxes that originated from the field on which the flux station was installed (field A or C).

2.5 Evaluation of the topographical slopes for the flux measurements

To understand the effects of relief on the energy fluxes, the topography near each flux station needed to be characterised, especially within the footprint area. Because the wind

406 direction fluctuated on a scale of 10 to 30 minutes, the terrain slopes for the dominant wind
407 directions needed to be evaluated within these time intervals. Thus, we calculated the terrain
408 slopes for all wind directions. The procedure was twofold.
409
410 First, we defined a rectangle centred on the flux station and oriented along a given
411 wind direction (yaw angle). The rectangle width was set to twice the median value of the
412 footprint width (the ellipsoid width across the wind direction, Section 2.4.4) and its length
413 was set to twice the median value of the footprint length (ellipsoid length along wind
414 direction, Section 2.4.4). We considered the median values of the footprint dimension twice to
415 account for the influence of the upstream / downstream relief on the flow structure. Once each
416 rectangle was defined, we extracted the corresponding altitude data from the DEM
417 (Section 2.3), and a topographical plane was fitted against the DEM data (i.e., the altitude
418 versus northing and easting coordinates). The topographical plane equation was next used to
419 calculate two terrain slopes geometrically similar to the angles given by the rotational
420 correction (Section 2.4.2): the along-wind slope corresponded to the pitch angle, and the
421 across-wind slope corresponded to the roll angle.
422
423 The above approach was chosen for three reasons: (1) it defined a wind-oriented
424 topography (along and across slopes); (2) these slopes were evaluated in a similar way to the
425 rotational correction characterising the airflow inclination; and (3) it accounted for the spatial
426 extent of the footprint area. The choice of a rectangle instead of an ellipsoid simplified the
427 calculations.
428
429 **3. RESULTS**
430
431 In this section we first analysed the meteorological data to characterise the
432 micrometeorological conditions, including the wind and convection regimes (Section 3.1).
433 Secondly, we analysed the results of the flux data quality control and the footprint estimates
434 (Section 3.2). Thirdly, we characterised the DEM-derived topographical slopes according to
435 the wind direction and then compared them against the airflow inclinations derived from the
436 rotational corrections of the EC data (Section 3.3). We finally addressed energy balance

437 closure (Section 3.4). These analyses were conducted by comparing the results obtained on
438 the two opposite rims of the catchment (e.g., over fields A and C).
439
440 **3.1 Climatic conditions**
441
442 3.1.1 Wind regime
443
444 The data from the meteorological station showed large wind speed values with a mean
445 daytime value of 4 m s^{-1} that was twice as large as the FAO mean value for more than 2000
446 sites around the world (Allen et al., 1998). These wind speed measurements closely agreed
447 with those collected by the sonic anemometers within fields A and C – the differences were
448 less than 1 m s^{-1}. This wind speed homogeneity was observed in previous studies conducted at
449 different locations within the Kamech catchment (Zitouna-Chebbi, 2009).
450
451 Fig. 4 presents the wind roses obtained from the data collected at the meteorological
452 station. These wind roses clearly show the existence of two dominant directions: winds
453 coming either from the northwest or from the south (actually south-southeast). This bi-modal
454 regime of northwest and south winds was observed throughout the experiment (years 2004
455 and 2006). At the daily timescale, no diurnal cycle was observed for the wind direction.
456
457 [Figure 4 about here]
458
459 To seek possible influences of wind direction on the turbulent fluxes, we distinguished
460 two dominant wind direction classes according to the observations displayed in Fig. 4
461 (clockwise degrees, north is 0°): winds coming from directions between the southwest (220°)
462 and east-northeast (70°), known hereafter as the northwest winds; and winds coming from the
463 other directions, known hereafter as south winds. For both 2004 and 2006, the proportions of
464 the northwest and south winds were 70% and 30%, respectively. These two dominant
465 directions were almost perpendicular to the valley axis (Fig. 2). Therefore, the northwest
466 winds induced simultaneous downward flows on the northern rim (Field A) and upward flows
467 on the southern rim (Field C). The reverse was observed with the south winds.
468

469 3.1.2 Micrometeorological conditions
470
471 As is typical for summer in the study site, rainfall amounts were notably low during
472 the experiments with a total amount of 1.5 mm for the data sets A06 and C06. A larger value
473 (81 mm) was observed for data set A04 because the experiment lasted until the beginning of
474 autumn (Section 2.1). The reference evapotranspiration (ET_0) was calculated from the data
475 collected at the meteorological station by following Allen et al. (1998). For the data set A04
476 (respectively A06 and C06), the ET_0 ranged between 1.4 and 10.4 mm per day (respectively
477 4.7 and 10.3 mm per day), with a mean value of 4.6 mm per day (respectively 6.6 mm per
478 day).
479
480 As expected for the day-time measurements under windy conditions (Section 3.1.1),
481 the Monin-Obukhov stability parameter (MOSP) was always negative, with notably few
482 values less than -0.1. For the northwest (respectively south) winds, the MOSP median values
483 were -0.042, -0.053 and -0.057 (respectively -0.059, -0.022 and -0.022) for the datasets A04,
484 A06 and C06. These values corresponded to the conditions of neutrality or low instability.
485
486 **3.2 Quality control and footprints of the EC data**
487
488 3.2.1 Quality control of the EC data
489
490 The results of the quality control test in Table 2 are given for the EC flux data after the
491 rotational correction. On average, 90% of the u_* and H fluxes reached the first quality class
492 for both the ST and ITC tests. For the latent heat flux, 70% of the data reached the first quality
493 class. The good results obtained with the ST test a posteriori justified the integration of the EC
494 data over the 30-minute intervals. The good results obtained with the ITC test showed that the
495 surface aerodynamic properties were spatially homogeneous near the flux stations, which was
496 in agreement with the bare soil conditions observed throughout the catchment during the
497 experiments.
498
499 [Table 2 about here]
500

501 The current study addressed the energy fluxes under sloping conditions within a hilly
502 catchment in the context of operationally monitoring crop water consumption under a semi-
503 arid climate. Thus, only the data belonging to the first two quality classes (ST and ITC test
504 values less than 1.0) were selected for further investigation. This represented 99% of the u_*
505 and H fluxes and 76% of the λE fluxes. Finally, we note applying rotational corrections
506 induced larger amounts of data fitting the quality control test, where the number of rotated
507 data in the first two quality classes increased by 40% relative to the number of non-rotated
508 data.
509
510 3.2.2 Footprints of the EC fluxes
511
512 The footprint areas were calculated using the EC flux data after the rotational
513 correction. For each 30-minute interval, the calculated footprint areas were superimposed on
514 the field map (Fig. 3), which allowed an evaluation of the percentage of fluxes originating
515 from the considered field. On average and regardless of wind direction, 55% (respectively
516 60%) of the flux measurements originated from Field A in 2004 (respectively 2006) and 80%
517 originated from Field C in 2006. Although these fields were selected as the best locations
518 within the catchment, these contributions were found to be moderate. However, this result
519 was not considered to be a critical issue because the surface conditions of the surrounding
520 fields were similar (bare soils), which was confirmed by the good results obtained with the
521 ITC test (Section 3.2.1).
522
523 The mono-modal distributions of the lengths and widths of the ellipsoid-shaped
524 footprints are given in Fig. 5. The median values of the footprint lengths were 208 m, 180 m
525 and 182 m for the A04, A06 and C06 data sets, respectively. The median values of the widths
526 were 62 m, 58 m and 58 m for the A04, A06 and C06 data sets, respectively. No significant
527 influence from the wind directions (northwest and south) was observed for the footprint
528 dimensions, with the differences between median lengths being less than 15% relative. This
529 was expected because the micrometeorological conditions did not significantly vary with the
530 wind direction.
531
532 [Figure 5 about here]

533

534 **3.3 Influence of the topography on the airflow inclination**

535

536 3.3.1 Determination of the terrain slopes from DEM data

537

538 According to the results from Section 3.2.2, the length of the rectangles used to
539 determine the terrain slopes from the DEM-based altitude data was fixed at 360 m, which is
540 twice the median value of the ellipsoid footprint lengths. The width of these rectangles was
541 fixed to 120 m, which was twice the median of the ellipsoid footprint widths.

542

543 The fitting of the terrain slopes for the south winds (yaw angle = 180° from north
544 clockwise) and the northwest winds (yaw angle = 320° from north clockwise) are illustrated
545 in Fig. 6, where the slanted thick lines represent the pitch angle calculated over the 360-m
546 long and 120-m wide rectangles (Section 2.5).

547

548 [Figure 6 about here]

549

550 In the vicinity of Field A, the topography at the 360-m scale appeared to be almost
551 planar for both the south and northwest winds. The top of the northern rim, which
552 corresponded to the catchment northwest limit (see Fig. 2), formed a sharp hill that is clearly
553 visible on Fig. 6 for the south winds (right vertical arrow at x = 290 m on top left subplot) and
554 for the northwest winds (left vertical arrow at x = -270 m on top right subplot). Field C had a
555 rugged relief with more dispersion of the altitude data and a less planar shape, especially for
556 the south winds. The hilltop at the field southern limit (x = -300 to -200 m on the bottom left
557 subplot, x = 150 m on the bottom right subplot) was rugged compared to the top of the
558 northern rim. The catchment southern limit was located 700 m south from Field C (left
559 vertical arrow on bottom left subplot, and right vertical arrow on bottom right subplot).

560

561 Following the illustrations from Fig. 6, the negative (respectively positive) angles
562 were allocated to the downward (respectively upward) flows. Fig. 7 displays the evolution of
563 the topographical pitch terrain slope and roll terrain slope with respect to the yaw angle. On
564 Field A, the pitch and roll terrain slopes ranged from 0 to 5.2° in absolute value, whereas they

565 ranged from 0 to 8.5° in absolute value on Field C, indicating a larger slope. As expected, the
566 pitch and roll terrain slopes were in phase quadrature for both fields. For a given field, we
567 observed different shapes for the pitch and roll curves. This finding was explained by the use
568 of a rectangle when extracting the DEM data to calculate the terrain slopes (Section 2.5 and
569 3.2.2), where the pitch angle corresponded to the rectangle length, whereas the roll angle
570 corresponded to the rectangle width. The quasi-sinusoidal shape observed for both the pitch
571 and roll terrain slopes on Field A confirmed its almost planar shape, whereas the more
572 complex evolution of the roll terrain slope on Field C corresponded to its rugged relief, as
573 already observed in Fig. 6.
574
575 [Figure 7 about here]
576
577 3.3.2 Comparison of the EC-based flow inclination against the DEM-based terrain slopes
578
579 The planar fit angle calculation for a given data set (A04, A06 and C06) was twofold,
580 either fitting a single plane over all of the data belonging to a wind sector (northwest or south)
581 or fitting a plane for each wind sector and each day (Section 2.4.2). The first calculation
582 yielded two planes corresponding to the northwest and south sectors for each data set. When
583 fitting a plane for each wind sector and each day, this calculation yielded between seven and
584 23 daily planes in accordance with the number of 30-minute intervals of 10-Hz data collected
585 (Section 2.2).
586
587 Fig. 8a and 8b display the evolution of the pitch and roll angles according to the yaw
588 angle when comparing the estimates from the DEM data and from the planar fit rotational
589 correction of the EC data. The continuous lines correspond to the DEM-derived topographical
590 slopes (Section 3.3.1). The discontinuous (dashed or dotted in accordance with year) lines
591 correspond to the planar fit derived slopes when considering a unique plane fitted over all data
592 belonging to a wind sector (northwest or south) for a given data set. In this case, pitch and roll
593 angles are calculated from the fitting plane by setting a 1° step range of the yaw angle values
594 that spread over the corresponding wind sector. The points are related to the planar fit-derived
595 slopes when considering each wind sector and each day.
596

[Figure 8a about here]

[Figure 8b about here]

For each data set (A04, A06, C06) and each wind sector (northwest, south) the planar fit estimates of pitch angles at the daily scale (symbols) were in close agreement with those calculated over the entire data sets (portions of broken curves). This result was explained by the bare soil conditions during the experiments, inducing little or no variation of the surface roughness. Thus, the daily evaluation of the planar fit-derived pitch angles appeared to be stable. For the planar fit-derived roll angles, a lower but correct agreement was observed between daily estimates and the averaged values over the experiment.

For the upward flows (positive values of the pitch angles), Fig. 8a shows an excellent agreement between the pitch slope estimates from the planar fit correction and from the DEM data. This agreement indicated that the airflow inclination, as captured by the planar fit correction, followed the along-wind topographical slope deduced from the DEM data. As indicated by the discontinuous lines, the differences between 2004 and 2006 for Field A were within 1.5°. For the downward flows (negative values of the pitch angles), the agreement was also excellent on Field C. A different behaviour was observed on Field A, where the planar fit-derived pitch angles were close to nil, varying between -2.5° and +1° in 2004 and between -1° and 0° in 2006. The inclination flow, as captured by the planar fit correction of the EC data, thus appeared to be almost horizontal.

Notably similar findings were found when comparing the roll angles deduced from the planar fit correction to those calculated from the DEM data, as observed on Fig. 8b. On Field C, the planar fit roll angles were in close agreement with the topography (within 2°) for all of the wind directions and for a large range of topographic slopes (±7°). On Field A, the planar fit roll angles were in good agreement with the topography (within 3°) under the upward flows and were close to nil (between -2° and +3.6°) under the downward flows. The difference between the planar fit roll angles obtained in 2004 and 2006 remained less than 3°.

628 Summarising the observations reported above: for the upward flows, the airflow pitch
629 (respectively roll) angles, as captured by the planar fit correction of the EC data, were in close
630 agreement with the topographical slope along (respectively across) the wind direction. For the
631 downward flows, the airflow pitch and roll angles were in close agreement with the
632 topographical slopes on Field C, whereas they tended toward being horizontal on Field A.
633
634 **3.4 Energy balance closure**
635
636 We analysed the energy balance closure by comparing the sum of convective energy
637 ($H+\lambda E$) against the available energy ($Rn-G$). The convective fluxes were those obtained from
638 the EC flux data after the rotational correction. Although the usefulness of such analysis as a
639 quality test may be debatable (Lee et al., 2004), it was considered an interesting comparison
640 of the independent measurements. The data to be compared were those calculated over the 30-
641 minute intervals (Section 2.2 and 2.4.2).
642
643 Given that no latent heat flux data were collected for the data set A06 because of the
644 krypton hygrometer inoperability, the energy balance closure could be analysed only for the
645 data sets A04 and C06. This issue was not critical because the previous observations noted for
646 the A06 data set were nearly identical to those noted for the A04 data set, when comparing the
647 planar fit angles against the terrain slopes (3.4.2). Next, the number of data involved in the
648 energy balance closure analysis resulted from several filters. First, the convective flux data
649 were filtered with quality control (Section 3.2.1). Second, an additional filter consisted of
650 removing the data that corresponded to the negative values for the available energy. Finally,
651 the number of available observations for assessing the energy balance closure was constrained
652 by the smallest data set among the net radiation, soil heat flux, sensible and latent heat flux.
653
654 The energy balance closure is graphically presented in Fig. 9, and the corresponding
655 statistics are given in Table 3. The energy balance closure, as expressed through the energy
656 balance ratio, ranged between 87 and 95%, with the exception of one case (the downward
657 flows on Field C in 2006) that corresponds to 73%. Regardless of the considered case (A04
658 and C06 data set, the upward and downward flows), the energy balance closure was
659 comparable to those found in the literature under various conditions, such as vegetated

660 canopies and bare soils under flat and mountainous conditions (Wilson et al., 2002; Hammerle
661 et al., 2007; Foken, 2008). We also observed from our data set that the available energy
662 systematically overestimated (respectively underestimated) the convective energy for large
663 (respectively low) values, which was also in agreement with the aforementioned literature.
664
665 [Figure 9 about here]
666
667 [Table 3 about here]
668
669 The 20–50 W m^{-2} error for the soil heat flux that resulted from neglecting the heat
670 storage between the surface and plates (Section 2.3) was not considered to be a critical issue.
671 Indeed, the resulting error had the same magnitude as the measurement uncertainty resulting
672 from the instrumental errors and spatial variability (Stannard et al., 1994; Kustas et al., 2000;
673 Olioso et al., 2002b; Shao et al., 2008). Most importantly, the energy balance closure reported
674 in this study was similar to those reported in previous studies that accounted for the heat
675 storage when measuring the soil heat flux (Wilson et al., 2002; Hammerle et al., 2007; Foken,
676 2008).
677
678 When analysing the energy balance closure as a function of the upward and downward
679 flows, the results for the energy balance closure were similar on Field A, but they were better
680 for the upward flow compared to the downward flow on Field C. On Field A, the systematic
681 errors were similar for the upward and downward flows with similar slope and offset values
682 for the linear regression of the convective energy against the available energy. The random
683 error was smaller for the upward flows (unsystematic root mean square error of 39.6 W m^{-2}
684 versus 47.4 W m^{-2}), but the energy balance residual (difference between available and
685 convective energy) was smaller for the downward flows (12.2 W m^{-2} versus 32.7 W m^{-2}). On
686 Field C, the random error was larger for the upward flows (unsystematic root mean square
687 error of 34.9 W m^{-2} versus 25.6 W m^{-2}), but the systematic error and the energy balance
688 residual were larger for downward flows (slope value of 0.64 versus 0.73; energy balance
689 residual of 81.2 W m^{-2} versus 26.9 W m^{-2}). The most important result for Field C was the
690 magnitude of the energy imbalance for the downward flows, approximately 27%, compared to
691 the other values, which ranged between 5% and 13%.

We finally analysed the impact of the rotational corrections on the energy balance closure to compare with previously published results. We expected our findings to increase our confidence in the EC measurements performed under the conditions of hilly topography. The planar fit correction increased the convective fluxes for the upward flows (between 5 and 50 W m^{-2} depending on the field, year and convective flux), whereas it decreased the convective fluxes for the downward flows, especially on Field C (by as much as 90 W m^{-2}). As expected, the magnitude of the planar fit correction was linked with the magnitude of the airflow inclination. Indeed, the horizontal airflows for the downward flows on Field A corresponded to the negligible planar fit correction for the convective fluxes. Furthermore, the planar fit correction was similar for the flux magnitude when comparing the two methods that we considered for calculating planar fit angles (Section 2.4.2), with differences of less than 10 W m^{-2} being observed. Finally, the energy balance closure was systematically improved after the planar fit correction (increase of EBR ratio values from 0.8 to 0.92 on average) apart from the downward flows on Field C.

4. DISCUSSION

For the wind regime, we had notably different findings when addressing the sloping effects within the Kamech hilly agricultural catchment compared to the previous studies that addressed slope effects within mountainous areas (Hammerle et al., 2007; Hiller et al., 2008). We did not observe the diurnal cycle of wind direction, anabatic and katabatic winds that blew up and down the slopes or the valley winds that followed the longitudinal axis of the catchment. This finding suggested the wind regime was externally driven and did not depend upon the local topography. We observed large wind speed values, which may be explained by the location of the catchment near the extremity of the Cap Bon Peninsula. The large wind speed values were in agreement with the micrometeorological data that indicated the dominant regimes of forced convection along with the conditions of near-neutrality or low instability.

When comparing the inclination flow derived from the planar fit correction of the EC measurements against the topographical slopes derived from the DEM data, different

724 situations were observed. For the upward flows, the planar fit angles were in notably good
725 agreement with the topographical slopes, which indicated that the airflow followed the terrain
726 slope along the wind direction. This result was observed on both fields A and C with the
727 different EC devices (Section 2.2) and on Field A for two different years (2004 and 2006).
728 For the downward flows, the planar fit angles were either in good agreement with the
729 topographical slope for Field C or were close to nil for Field A.
730
731 The differences we observed between the upward and downward flows were not
732 ascribed to the differences in the meteorological or micrometeorological conditions. Because
733 the EC data were collected over two opposite sides of the watershed, the upward flows on a
734 given side correspond to the downward flows on the opposite side for the same
735 meteorological conditions and wind direction.
736
737 The verticality of the EC devices could not be set and controlled numerically.
738 Nevertheless, the resulting inaccuracy of the alignment of the EC devices could not weaken
739 the findings on the change in flow inclination according to the upward and downward flows.
740 First, the same behaviour was observed in Field A in 2004 and 2006, where the agreement
741 between the flow inclination and topographical slope was good despite small differences in
742 the flow inclination between 2004 and 2006 (Fig. 8a and 8b). Second, the error of the
743 alignment for each EC device did not affect the relative difference between the flow
744 inclination for the upward and downward flows; this difference remained unchanged
745 regardless of the EC alignment.
746
747 When comparing the airflow inclinations against the topographical slopes for the
748 downward flows, the abovementioned differences between fields A and C were ascribed to
749 the topographical conditions. The hillslope geometries were different because Field A
750 depicted a twofold-lower ratio of the altitude difference to the length (0.1 versus 0.2) (Fig. 6),
751 where this ratio is similar to the ratio of height to the half-length commonly used to
752 characterise the flows over hills (Raupach and Finnigan 1997, Finnigan and Belcher 2004).
753 These differences in the hillslope geometries were combined with differences in the locations
754 of the EC flux stations within the hillslopes, closer to the rim top than to the valley bottom on
755 Field A (top right subplot of Fig. 6 for northwest winds) and conversely for Field C (bottom

left subplot of Fig. 6 for south winds). Thus, the EC flux stations had different locations within the separation bubble that is characterised by the airflow variability (Raupach and Finnigan 1997, Belcher et al., 2008). Furthermore, asymmetry between the upward and downward flows, as observed on Field A but not on Field C, was also reported by Finnigan and Belcher (2004). However, a comparison with the outcomes from such modelling studies should be substantiated. First, these modelling studies addressed the downward flows within the lee of the hill without any obstacle from the downstream topography. Second, the downward flows that we addressed in this study were in equilibrium with the downstream topography induced by the opposite rim of the catchment.

Apart from the downward flows of Field C, the energy balance closure was similar in all of the cases and improved after the application of the planar fit correction. Both findings were similar to those reported in the literature (Wilson et al., 2002, Hammerle et al., 2007; Foken, 2008). The available energy tended to overestimate the convective energy, as reported by Foken (2008). The worse results for Field C may be explained by the location of the EC flux station on the hillslope. Indeed, Finnigan (2004) suggested the location of the flux station relative to the hilltop is critical for flux accuracy, which depends upon the wind direction.

Overall, applying the rotational correction improved both the data filtering and the energy balance closure. This result was in agreement with the outcomes from other studies that mainly focused on flat or mountainous conditions. Such agreement was considered as an indicator of the data consistency and reliability. This is an important outcome for the data collected under these specific conditions that has been barely addressed until now (i.e., hilly topography).

Analysis of the results was conducted by differentiating the upward and downward flows. According to this analysis, the upward flows appeared to induce behaviours similar to those observed under flat conditions. Indeed, streamlines followed the local topography, whereas the energy balance was improved after the planar fit correction that increased the fluxes. Different behaviour was observed for the downward flows, possibly induced by the streamline dilatation and reverse circulation flow (Raupach and Finnigan 1997; Belcher et al., 2008). Furthermore, the results were worse for Field C, which may be explained by the

788 complex topography of the southern rim. First, the rugged topography may induce complex
789 turbulence structures; second, the rugged topography induced differences in the solar heating
790 for bare soils, which may result in horizontal advection.
791
792 **5. CONCLUDING REMARKS**
793
794 Hilly catchments are widespread throughout the world. In arid and semi-arid climates,
795 they have socioeconomic implications with regard to water harvesting for agricultural
796 production. Our understanding of surface fluxes within such areas must be improved in the
797 context of operational monitoring and modelling for decision-support purposes. The current
798 paper offered insights regarding energy fluxes from a hilly catchment under bare soil
799 conditions, but further research is needed. Beyond the previous studies that addressed sloping
800 terrain vegetated with tall canopies (e.g., forests); the fluxes over agricultural canopies must
801 also be investigated. Indeed, vegetation is known to affect the pressure gradient associated
802 with the flow over hills (Finnigan and Brunet, 1995, Finnigan and Belcher, 2004) and thus to
803 influence the airflow and surface fluxes (Raupach and Finnigan, 1997; Turnipseed et al.,
804 2003). Furthermore, these vegetation effects may combine with the topography and wind
805 direction. Finally, the aerodynamic implications must be emphasised, where the roughness
806 length should be revisited relative to the asymmetry between the upward and downward
807 airflows, as suggested by Finnigan and Belcher (2004). This approach will enable the
808 expansion of the recent modelling works (Rana et al., 2007) with implications for the
809 operational FAO-56 method (Allen et al., 1998).
810
811 **Acknowledgments**
812
813 Financial support for this study was provided by (1) the French Institute of Research
814 for Development (IRD) through the Department for Support and Training and through the
815 Environmental Research Observatory OMERE; (2) the European Union (Seventh Framework
816 Programme) through the IRRIMED project (contract ICA3-2002-10080); and (3) the
817 Agropolis Foundation (Thematic Network of Advanced Research "Montpellier Agronomy
818 and Sustainable Development") through the "Land surface atmosphere exchanges within hilly
819 watersheds" project (contract 0901-013). The authors wish to thank Henk de Bruin and Oscar

820 Hartogensis for their technical support in processing the EC data. We give warm thanks to
821 Yves Brunet for the constructive criticism of the manuscript and for the subsequent
822 discussions. We are also grateful to John Gash for manuscript edition. This paper is dedicated
823 to the memory of Raoudha Mougou.
824
825 **References**
826
827 Allen, R.G., Pereira, L.S., Raes, D., Smith, M., 1998. Crop evapotranspiration: guidelines for
828 computing crop water requirements. FAO Irrigation and Drainage Paper No. 56, FAO, Rome,
829 300pp.
830
831 Belcher, S.E., Finnigan, J.J., Harman, I.N., 2008. Flows through forest canopies in complex
832 terrain. Ecol. Appl. 18 (6), 1436-1453.
833
834 Brunet, Y., Finnigan, J.J., Raupach, M.R., 1994. A Wind-Tunnel Study of Air-Flow in
835 Waving Wheat - Single-Point Velocity Statistics. Boundary-Layer Meteorol. 70 (1-2), 95-132.
836
837 Collares-Pereira, M., Rabl, A., 1979. The average distribution of solar radiation—correlations
838 between diffuse and hemispherical and between daily and hourly insolation values. Sol.
839 Energy 22, 155–164.
840
841 Courault, D., Seguin, B., Olioso, A., 2005. Review on estimation of evapotranspiration from
842 remote sensing data: From empirical to numerical modeling approaches. Irrig. Drain. Syst. 19
843 (3), 223-249.
844
845 Daneshkar Arasteh, P., Tajrishy, M., 2008. Calibrating Priestley-Taylor Model to Estimate
846 Open Water Evaporation under Regional Advection Using Volume Balance Method-Case
847 Study: Chahnimeh Reservoir, Iran. J. Appl. Sci. 8 (22), 4097-4104.
848
849 Dupont, S., Brunet, Y., Finnigan, J.J., 2008. Large-eddy simulation of turbulent flow over a
850 forested hill: Validation and coherent structure identification. Quart. J. Roy. Meteorol. Soc.
851 134 (636), 1911-1929.

Feigenwinter, C., Bernhofer, C., Eichelmann, U., Heinesch, B., Hertel, M., Janous, D., Kolle, O., Lagergren, F., Lindroth, A., Minerbi, S., Moderow, U., Mölder, M., Montagnani, L., Queck, R., Rebmann, C., Vestin, P., Yernaux, M., Zeri, M., Ziegler, W., Aubinet, M., 2008. Comparison of horizontal and vertical advective CO2 fluxes at three forest sites. Agric. For. Meteorol. 148(1), 12-24.

Finnigan, J.J., Brunet, Y., 1995. Turbulent airflow in forests on flat and hilly terrain. In: Coutts, M.P., Grace, J. (Eds.), Wind and Trees. Cambridge University Press, UK, pp. 3-40.

Finnigan, J.J., 2004. Advection and modelling. In: Lee, X., Massman, W., Law, B. (Eds.), Handbook of Micrometeorology: A Guide for Surface Flux Measurement and Analysis. Kluwer Academic Publisher, Dordrecht, pp. 209–241.

Finnigan, J.J., Belcher, S.E., 2004. Flow over a hill covered with a plant canopy. Quart. J. Roy. Meteorol. Soc. 130 (596), 1-29.

Foken, T., Wichura, B., 1996. Tools for quality assessment of surface-based flux measurements. Agric. For. Meteorol. 78(1-2), 83-105.

Foken, T., Gockede, M., Mauder, M., Mahrt, L., Amiro, B., Munger, W., 2004. Post-field data quality control. In: Lee, X., Massman, W., Law, B. (Eds.), Handbook of Micrometeorology: A Guide for Surface Flux Measurement and Analysis. Kluwer Academic Publisher, Dordrecht, pp. 181–208.

Foken, T., 2008. The energy balance closure problem - An overview. Ecol. Appl. 18 (6), 1351-1367.

Geissbühler, P., Siegwolf, R., Eugster, W., 2000. Eddy covariance measurements on mountain slopes: The advantage of surface-normal sensor orientation over a vertical set-up. Boundary-Layer Meteorol. 96 (3), 371-392.

884 Hammerle, A., Haslwanter, A., Schmitt, M., Bahn, M., Tappeiner, U., Cernusca,
885 A., Wohlfahrt, G., 2007. Eddy covariance measurements of carbon dioxide, latent and
886 sensible energy fluxes above a meadow on a mountain slope. Boundary-Layer Meteorol. 122
887 (2), 397-416.
888
889 Heusinkveld, B.G., Jacobs, A.F.G., Holtslag, A.A.M., Berkowicz, S.M., 2004. Surface energy
890 balance closure in an arid region: role of soil heat flux. Agric. Forest Meteorol. 122, 21–37.
891
892 Hiller, R., Zeeman, M.J., Eugster, W., 2008. Eddy-covariance flux measurements in the
893 complex terrain of an Alpine valley in Switzerland. Boundary-Layer Meteorol. 127 (3), 449-
894 467.
895
896 Holst, T., Rost, J., Mayer, H., 2005. Net radiation balance for two forested slopes on opposite
897 sides of a valley. Int. J. Biometeorol. 49, 275-284.
898
899 Horst, T.W., Weil, J.C., 1992. Footprint Estimation for Scalar Flux Measurements in the
900 Atmospheric Surface-Layer. Boundary-Layer Meteorol. 59 (3), 279-296.
901
902 Humphreys, E.R., Black, T.A., Ethier, G.J., Drewitt, G.B., Spittlehouse, D.L., Jork, E.-
903 M., Nesic, Z., Livingston, N.J., 2003. Annual and seasonal variability of sensible and latent
904 heat fluxes above a coastal Douglas-fir forest, British Columbia, Canada. Agric. For.
905 Meteorol. 115 (1-2), 109-125.
906
907 Hunt, J.C.R., Leibovich, S., Richards, K.J., 1988. Turbulent Shear Flows over Low Hills.
908 Quart. J. Roy. Meteorol. Soc. 114 (484), 1435-1470.
909
910 Jackson, P.S., Hunt, J.C.R., 1975. Turbulent Wind Flow over a Low Hill. Quart. J. Roy.
911 Meteorol. Soc. 101(430), 929-955.
912
913 Kaimal, J.S., Finnigan, J.J., 1994. Atmospheric boundary layer flows, their structure and
914 measurement. Oxford university press, Oxford, 289 pp.
915

916 Kustas, W.P., Humes, K.S., Norman, J.M., Moran, M.S., 1996. Single-and dual-source
917 modeling of surface energy fluxes with radiometric surface temperature. J. Appl. Meteorol.
918 35, 110-121.
919
920 Kustas, W.P., Prueger, J.H., Hatfield, J.L., Ramalingam, K., Hipps, L.E., 2000. Variability in
921 soil heat flux from a mesquite dune site. Agric. For. Meteorol. 103, 249-264.
922
923 Lee, X., Finnigan, J.J., Paw U, K.T., 2004. Coordinate systems and flux bias error. In: Lee,
924 X., Massman, W.J., Law, B. (Eds.), Handbook of micrometeorology. A guide for surface flux
925 measurements and analysis. Kluwe academic publishers, pp. 33-64.
926
927 Lewicki, J.L., Fischer, M.L., Hilley, G.E., 2008. Six-week time series of eddy covariance
928 CO2 flux at Mammoth Mountain, California: Performance evaluation and role of
929 meteorological forcing. J. Volcanol. Geotherm. Res. 171 (3-4), 178-190.
930
931 Liebethal, C., Huwe, B., Foken, T., 2005. Sensitivity analysis for two ground heat flux
932 calculation approaches. Agric. For. Meteorol. 132, 253-262.
933
934 Massman, W.J., Lee, X., 2002. Eddy covariance flux corrections and uncertainties in long-
935 term studies of carbon and energy exchanges. Agric. For. Meteorol. 113 (1-4), 121-144.
936
937 Mekki, I., Albergel, J., Ben Mechlia, N., Voltz, M., 2006. Assessment of overland flow
938 variation and blue water production in a farmed semi-arid water harvesting catchment. Phys.
939 Chem. Earth. 31 (17), 1048-1061.
940
941 Moussa, R., Chahinian, N., Bocquillon, C., 2007. Distributed hydrological modelling of a
942 Mediterranean mountainous catchment - model construction and multi-site validation. J.
943 Hydrol. 337 (1-2), 35-51.
944
945 Olioso, A., Braud, I., Chanzy, A., Courault, D., Demarty, J., Kergoat, L., Lewan, E., Ottlé,
946 C., Prévot, L., Zhao, W. G., Calvet, J.-C., Cayrol, P., Jongschaap, R., Moulin, S., Noilhan,

947 J., Wigneron, J.P., 2002a. SVAT modeling over the Alpilles-ReSeDA experiment: comparing
948 SVAT models over wheat fields. Agron. Sustainable Dev. 22 (6), 651-668.
949
950 Olioso, A., Braud, I., Chanzy, A., Demarty, J., Ducros, Y., Gaudu, J.-C., Gonzalez-Sosa,
951 E., Lewan, E., Marloie, O., Ottlé, C., Prévot, L., Thony, J.-L., Autret, H., Bethenod,
952 O., Bonnefond, J.-M., Bruguier, N., Buis, J.-P., Calvet, J.-C., Caselles, V., Chauki, H., Coll,
953 C., François, C., Goujet, R., Jongcshaap, R., Kerr, Y., King, C., Lagouarde, J.-P., Laurent, J.-
954 P., Lecharpentier, P., McAneney, J., Moulin, S., Rubio, E., Weiss, M., Wigneron, J.-P.,
955 2002b. Monitoring energy and mass transfers during the Alpilles-ReSeDA experiment.
956 Agron. Sustainable Dev. 22 (6), 597-610.
957
958 Poggi, D., Katul, G., 2007. An experimental investigation of the mean momentum budget
959 inside dense canopies on narrow gentle hilly terrain. Agric. For. Meteorol. 144 (1-2), 1-13.
960
961 Raclot, D., Albergel, J., 2006. Runoff and water erosion modelling using WEPP on a
962 Mediterranean cultivated catchment. Phys. Chem. Earth. 31 (17), 1038-1047.
963
964 Rana, G., Katerji, N., 2000. Measurement and estimation of actual evapotranspiration in the
965 field under Mediterranean climate: a review. Eur. J. Agron. 13 (2-3), 125-153.
966
967 Rana, G., Ferrara, R.M., Martinelli, N., Personnic, P., Cellier, P., 2007. Estimating energy
968 fluxes from sloping crops using standard agrometeorological measurements and topography.
969 Agric. For. Meteorol. 146 (3-4), 116-133.
970
971 Raupach, M.R., Weng, W.S., Carruthers, D.J., Hunt, J.C.R., 1992. Temperature and Humidity
972 Fields and Fluxes over Low Hills. Quart. J. Roy. Meteorol. Soc. 118 (504), 191-225.
973
974 Raupach, M.R., Finnigan, J.J., 1997. The influence of topography on meteorological variables
975 and surface-atmosphere interactions, J. Hydrol. 190 (3-4), 182-213.
976
977 Rebmann, C., Göckede, M., Foken, T., Aubinet, M., Aurela, M., Berbigier, P., Bernhofer, C.,
978 Buchmann, N., Carrara, A., Cescatti, A., Ceulemans, R., Clement, R., Elbers, J.A., Granier,

A., Grünwald, T., Guyon, D., Havránková, K., Heinesch, B., Knohl, A., Laurila, T., Longdoz, B., Marcolla, B., Markkanen, T., Miglietta, F., Moncrieff, J., Montagnani, L., Moors, E., Nardino, M., Ourcival, J.M., Rambal, S., Rannik, U., Rotenberg, E., Sedlak, P., Unterhuber, G., Vesala, T., Yakir, D., 2005. Quality analysis applied on eddy covariance measurements at complex forest sites using footprint modelling, Theor. Appl. Climatol. 80 (2-4), 121-141.

Saha, R., Ghosh, P.K., Mishra, V.K., Bujarbaruah, K.M., 2007. Low-cost micro-rainwater harvesting technology (Jalkund) for new livelihood of rural hill farmers. Curr. Sci. 29 (9), 1258-1265.

Scott, R.L., 2010. Using watershed water balance to evaluate the accuracy of eddy covariance evaporation measurements for three semiarid ecosystems. Agric. For. Meteorol. 150 (2), 219-225.

Shao, C.L., Chen, J.Q., Li, L.H., Xu, W.T., Chen, S.P., Gwen, T., Xu, J.Y., Zhang, W.L., 2008. Spatial variability in soil heat flux at three Inner Mongolia steppe ecosystems. Agric. For. Meteorol. 148, 1433–1443.

Stannard, D.I., Blanford, J.H., Kustas, W.P., Nichols, W.D., Amer, S.A., Schmugge, T.J., Weltz, M.A., 1994. Interpretation of surface fluxes measurements in heterogeneous terrain during the Monsoon ’90 experiment. Water Resour. Res. 30(5), 1227-1239.

Tamura, T., Cao, S., Okuno, A., 2007. LES study of turbulent boundary layer over a smooth and a rough 2D hill model. Flow, Turbul. Combust. 79 (4), 405-432.

Turnipseed, A.A., Anderson, D.E., Blanken, P.D., Baugh, W.M., Monson, R.K., 2003. Airflows and turbulent flux measurements in mountainous terrain Part 1. Canopy and local effects. Agric. For. Meteorol. 119 (1-2), 1-21.

van-Dijk, A., Moene, A.F., DeBruin, H.A.R., 2004. The principles of surface flux physics: theory, practice and description of the ECPACK library. Internal report 2004/1, Meteorology and Air Quality Group, the Netherlands, Wageningen, the Netherlands 99 pp.

1011
1012 Wilczak, J.M., Oncley, S.P., Stage, S.A., 2001. Sonic anemometer tilt correction algorithms.
1013 Boundary-Layer Meteorol. 99 (1), 127-150.
1014
1015 Wilson, K., Goldstein, A., Falge, F., Aubinet, M., Baldocchi, D., Berbigier, P., Bernhofer,
1016 C., Ceulemans, R., Dolman, H., Field, C., Grelle, A., Ibrom, A., Law, B.E., Kowalski,
1017 A., Meyers, T., Moncrieff, J., Monson, R., Oechel, W., Tenhunen, J., Valentini, R., Verma, S.,
1018 2002. Energy balance closure at FLUXNET sites. Agric. For. Meteorol. 113 (1-4), 223-243.
1019
1020 Zitouna Chebbi, R., 2009. Observing and characterising water and energy exchanges within
1021 the soil-plant-atmosphere continuum under condition of hilly relief. The case study of the
1022 Kamech catchment, Cap Bon Peninsula, Tunisia. Ph.D. thesis from the Montpellier SupAgro
1023 graduate School of Agronomy, Montpellier, France 292 pp.
1024
1025

Figure captions

Figure 1: Location of Tunisia within the Mediterranean Basin (top); location the Kamech catchment within the Cap Bon Peninsula, northeastern Tunisia (bottom left); and a three-dimensional view of the Kamech catchment with the corresponding perimeter in white (bottom right).

Figure 2: Topography of the Kamech catchment deduced from a 4-m spatial resolution digital elevation model (DEM). Altitude above sea level is given in metres (right greyscale bar). The thick black line represents the catchment outline. The altitude contour lines (thin black lines) are drawn every 10 m. The positions of the meteorological station (M) and of the flux stations on fields A and C are represented by the white circles.

Figure 3: Detailed view of the topography near fields A and C within the Kamech catchment. Altitude above sea level is given in metres (right greyscale bar). The thick black lines represent the field limits. The altitude contour lines (thin black lines) are drawn every 5 m. The positions of the flux stations are represented by white circles.

Figure 4: Distribution of the wind direction throughout the experiment for the years 2004 (left) and 2006 (right). The two wind roses indicate the occurrence of wind speeds for 16 wind directions.

Figure 5: Distributions of the footprint dimensions for the fields A (top line; datasets A04 and A06 are merged) and C (bottom line; dataset C06). The footprint lengths (along the wind direction) are in the left column, and the footprint widths (across the wind direction) are in the right column. Median values are indicated by vertical black lines. Footprint dimensions (x-axis) are in metres. The y-axis is the number of 30-minute intervals belonging to each class.

Figure 6: Determination of the wind-oriented topography for fields A (top line) and C (bottom line), for the south winds (left column, yaw angle = 180° from north clockwise) and northwest winds (right column, yaw angle = 320° from north clockwise). The points are the DEM-derived altitude data extracted within a 120-m-wide rectangle, oriented along each wind direction (S or NW) and passing through the flux stations (A or C). The x-axis is the distance from the flux stations (x=0, vertical dotted line) along the wind direction, where the wind blows from the negative to positive x values (metres). The y-axis is the altitude above sea level (metres). The vertical arrows represent the limits of the catchment. A topographical plane was fitted against these altitude data for determining the wind oriented topographical slopes equivalent to the planar fit pitch and roll angles. The thick lines represent the along-wind (pitch) slopes calculated with a 360-m-long and 120-m-wide wind-oriented rectangle. The insets are zoom-ins centred on each field, showing the local topography.

Figure 7: Evolution of the wind-oriented topography (along-wind slope – equivalent to pitch angle – and across wind slope – equivalent to roll angles – on y-axis) with respect to the wind direction (yaw angle as x-axis, 0° is north, 90° is east) for fields A (thick lines) and C (thin lines). The solid lines represent the pitch angles, and the dashed lines represent the roll angles. The slope angles are calculated with a 1° yaw angle step.

Figure 8a: Compared evolution of the planar fit derived pitch angles and the topographical along-wind slopes (y-axis) with respect to the wind direction (x-axis, 0° is north, 90° is east) for fields A (top) and C (bottom). The continuous curves represent the topographical along-wind slope, as derived from the DEM data (same as Fig. 7). The planar fit-derived pitch angles evaluated over the entire datasets (A04, A06, C06) and for each wind sector (south and northwest) are represented by the portions of discontinuous curves (dotted lines for year 2004, dashed lines for year 2006); they are labelled as the "PF mean pitch". The planar fit-derived pitch angles evaluated for each day and each wind sector are represented by symbols (triangles for the year 2004, circles for the year 2006), where each symbol represents a day or a portion of the day during which the wind direction was within a wind sector; they are labelled as the "PF pitch".

Figure 8b: Compared evolution of the planar fit derived roll angles and topographical cross-wind slopes (y-axis) with respect to the wind direction (x-axis, 0° is north, 90° is east) for fields A (top) and C (bottom). The continuous curves represent the topographical across-wind slope, as derived from the DEM data (same as Fig. 7). The planar fit-derived roll angles evaluated over the entire datasets (A04, A06, C06) and for each wind sector (south and northwest) are represented by the portions of the discontinuous curves (dotted lines for the year 2004, dashed lines for the year 2006); they are labelled as the "PF mean roll". The planar fit-derived roll angles evaluated for each day and each wind sector are represented by symbols (triangles for the year 2004, circles for the year 2006), where each symbol represents a day or a portion of the day during which the wind direction was within a wind sector; they are labelled as the "PF roll".

Figure 9: Energy balance closure for the datasets A04 (top line) and C06 (bottom line) and for the upward winds (left column) and downward winds (right column). The available energy Rn-G (W m^{-2}) is on the x-axis, and the convective energy H+LE (W m^{-2}) is on the y-axis. The data correspond to the 30-minute intervals. The dashed line is the 1:1 line, and the continuous line is the y-axis data versus x-axis data regression line (regression coefficients are given in Table 3).

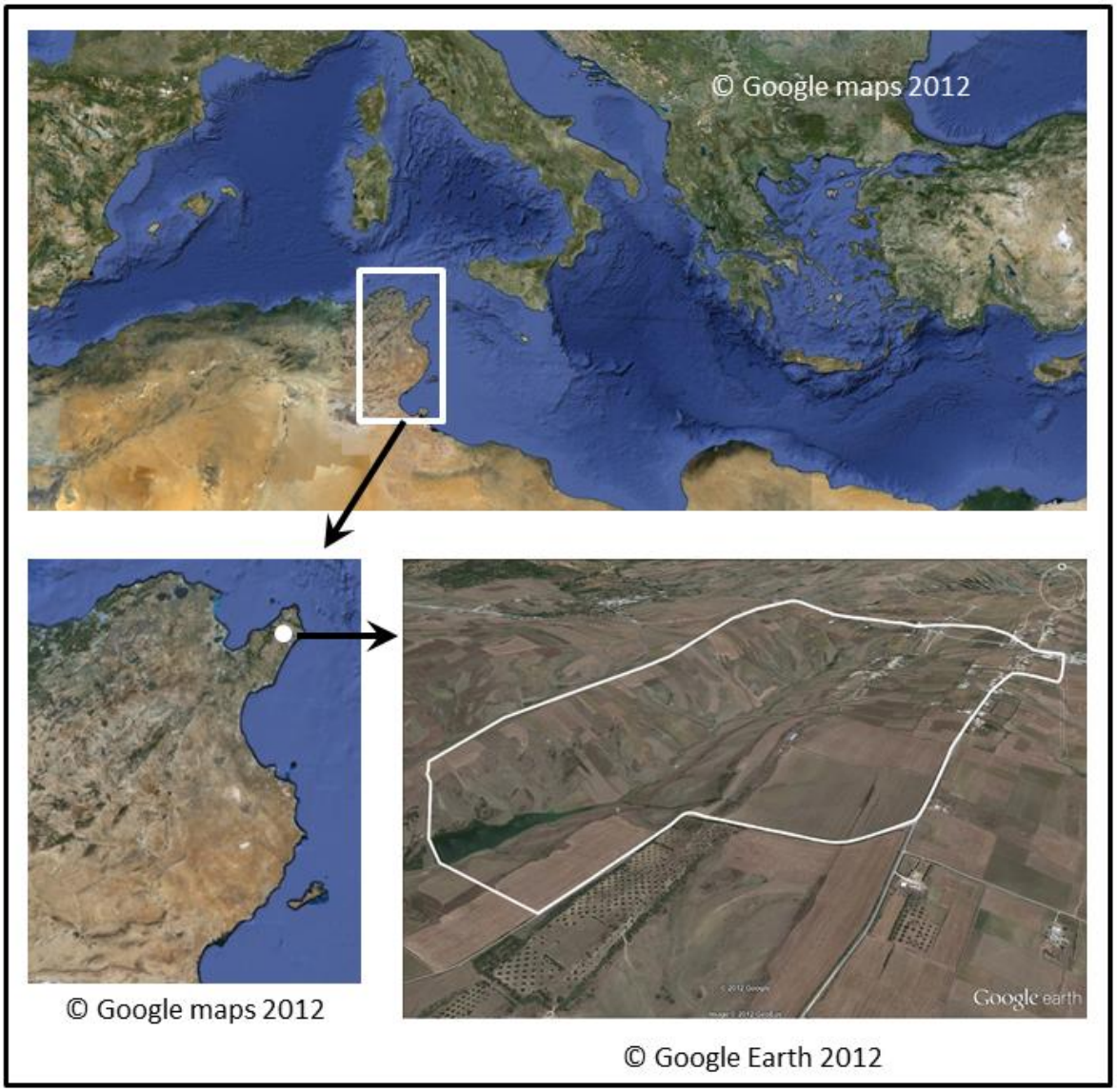

Figure 1: Location of Tunisia within the Mediterranean Basin (top); location the Kamech catchment within the Cap Bon Peninsula, northeastern Tunisia (bottom left); and a three-dimensional view of the Kamech catchment with the corresponding perimeter in white (bottom right).

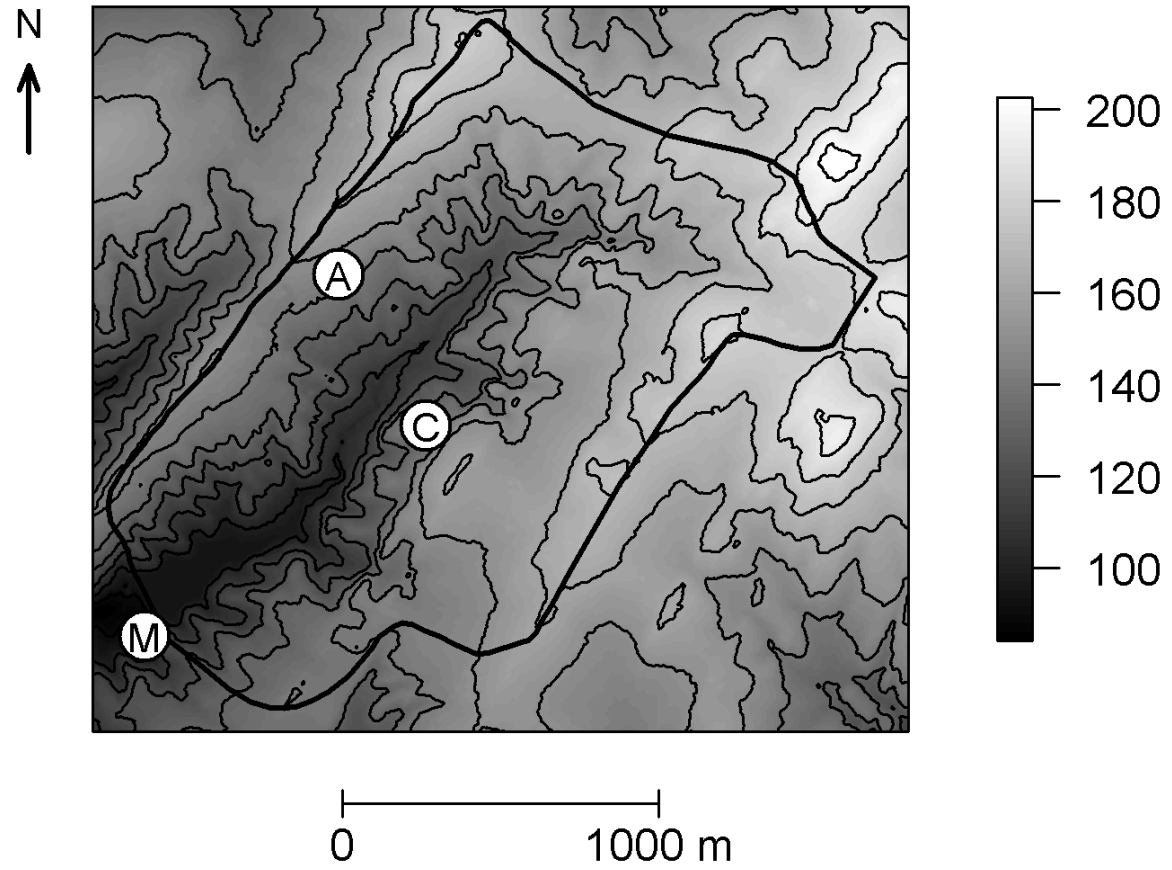

Figure 2: Topography of the Kamech catchment deduced from a 4-m spatial resolution digital elevation model (DEM). Altitude above sea level is given in metres (right greyscale bar). The thick black line represents the catchment outline. The altitude contour lines (thin black lines) are drawn every 10 m. The positions of the meteorological station (M) and of the flux stations on fields A and C are represented by the white circles.

1123

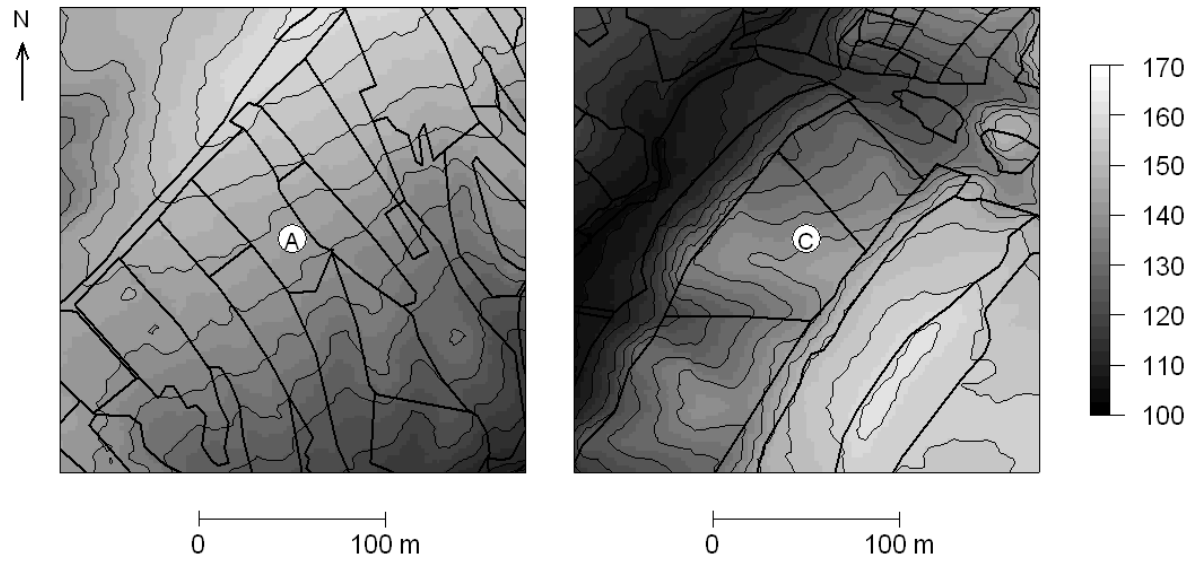

1124
1125
1126 Figure 3: Detailed view of the topography near fields A and C within the Kamech catchment.
1127 Altitude above sea level is given in metres (right greyscale bar). The thick black lines
1128 represent the field limits. The altitude contour lines (thin black lines) are drawn every 5 m.
1129 The positions of the flux stations are represented by white circles.
1130
1131

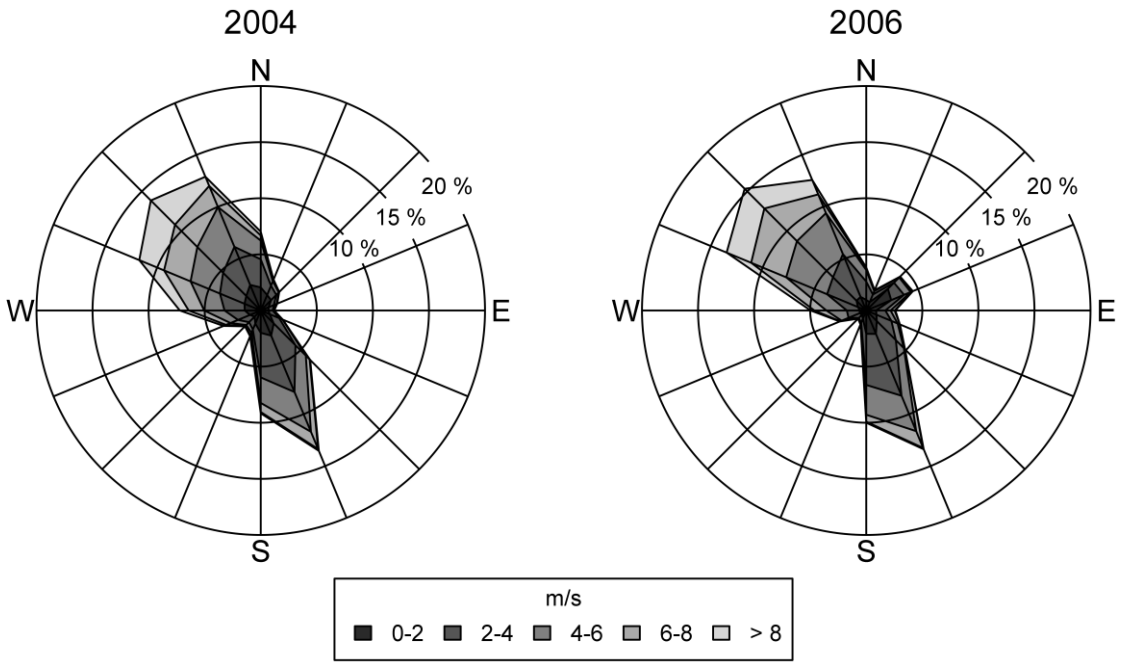

Figure 4: Distribution of the wind direction throughout the experiment for the years 2004 (left) and 2006 (right). The two wind roses indicate the occurrence of wind speeds for 16 wind directions.

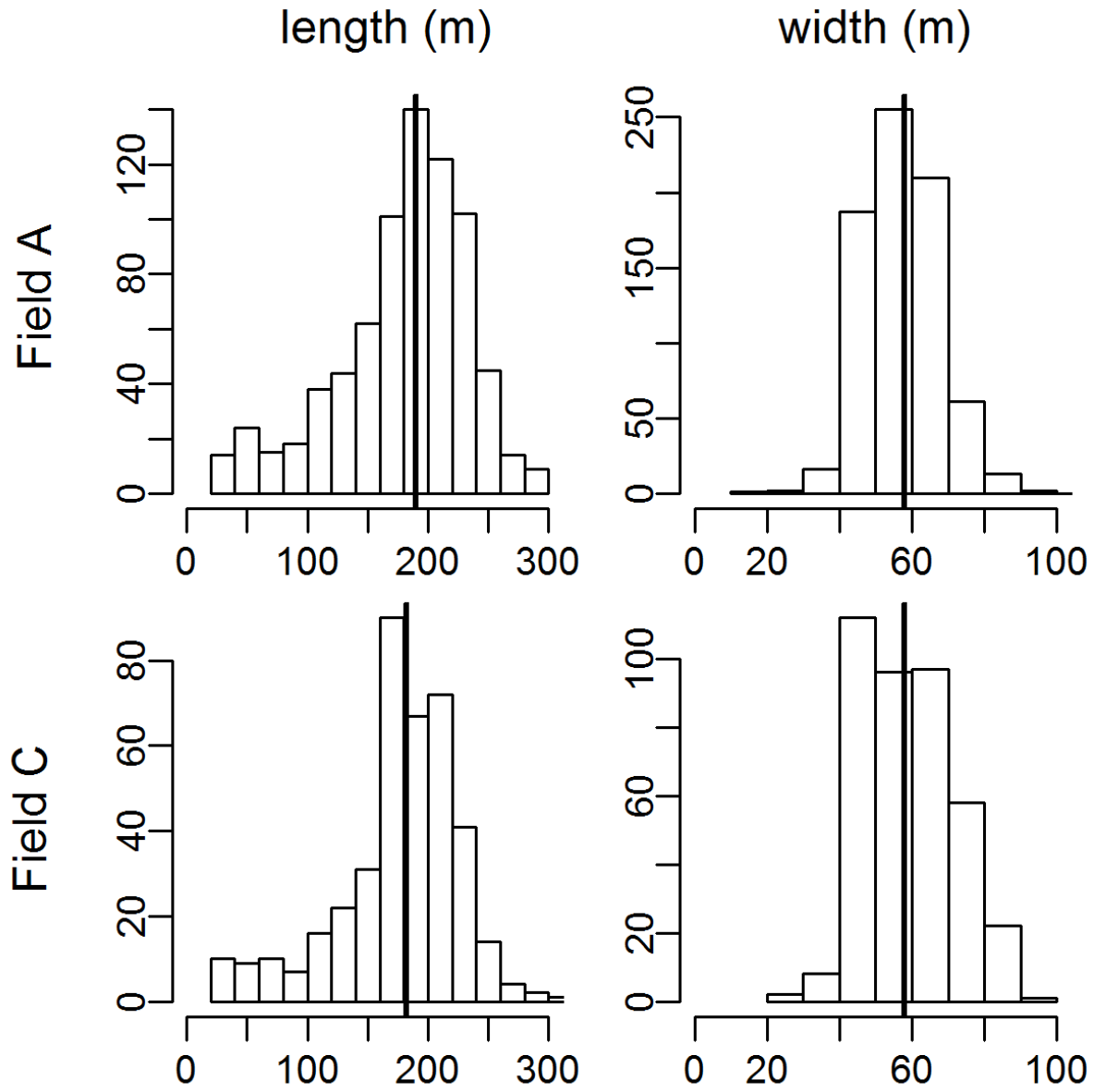

Figure 5: Distributions of the footprint dimensions for the fields A (top line; datasets A04 and A06 are merged) and C (bottom line; dataset C06). The footprint lengths (along the wind direction) are in the left column, and the footprint widths (across the wind direction) are in the right column. Median values are indicated by vertical black lines. Footprint dimensions (x-axis) are in metres. The y-axis is the number of 30-minute intervals belonging to each class.

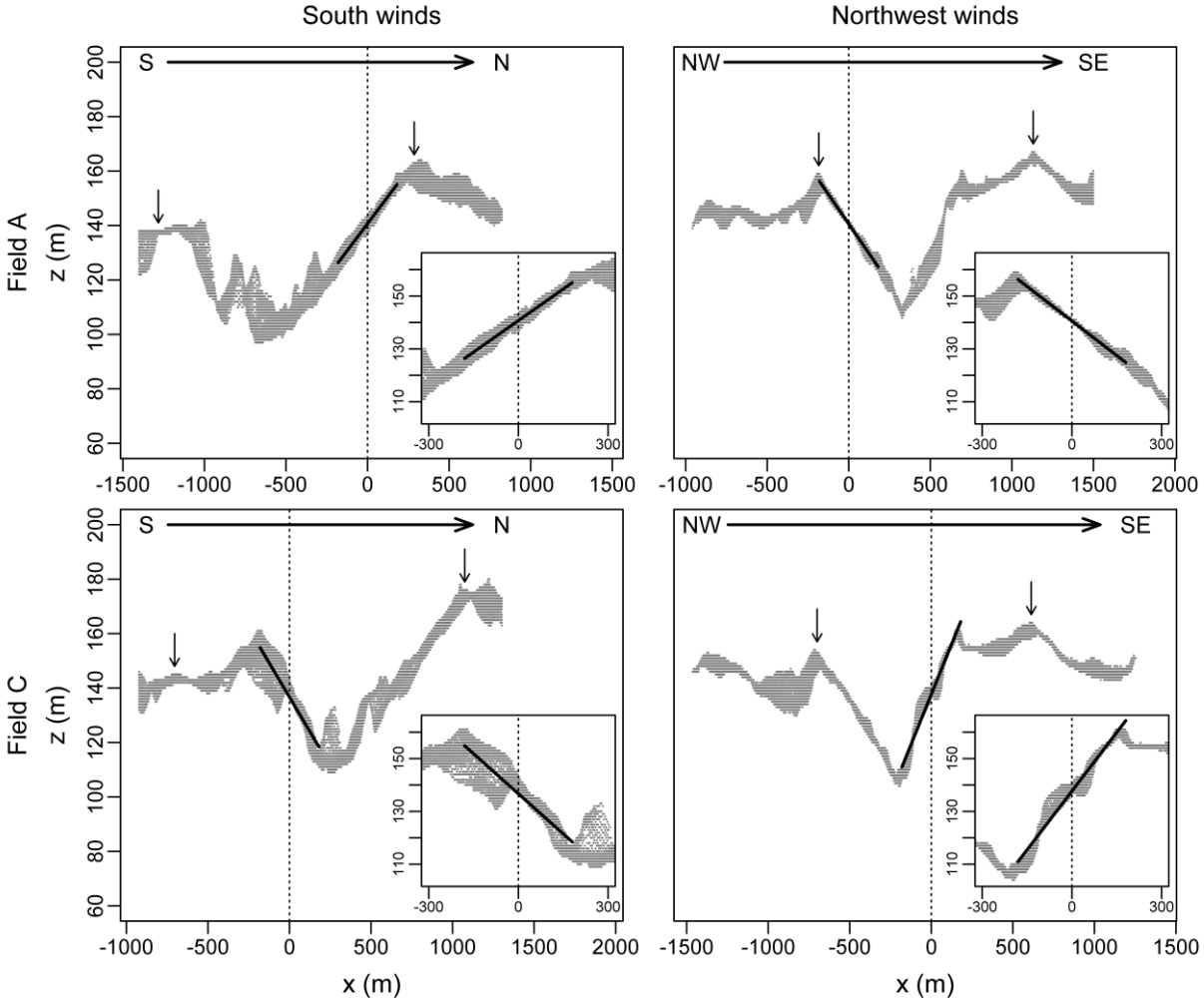

Figure 6: Determination of the wind-oriented topography for fields A (top line) and C (bottom line), for the south winds (left column, yaw angle = 180° from north clockwise) and northwest winds (right column, yaw angle = 320° from north clockwise). The points are the DEM-derived altitude data extracted within a 120-m-wide rectangle, oriented along each wind direction (S or NW) and passing through the flux stations (A or C). The x-axis is the distance from the flux stations (x=0, vertical dotted line) along the wind direction, where the wind blows from the negative to positive x values (metres). The y-axis is the altitude above sea level (metres). The vertical arrows represent the limits of the catchment. A topographical plane was fitted against these altitude data for determining the wind oriented topographical slopes equivalent to the planar fit pitch and roll angles. The thick lines represent the along-wind (pitch) slopes calculated with a 360-m-long and 120-m-wide wind-oriented rectangle. The insets are zoom-ins centred on each field, showing the local topography.

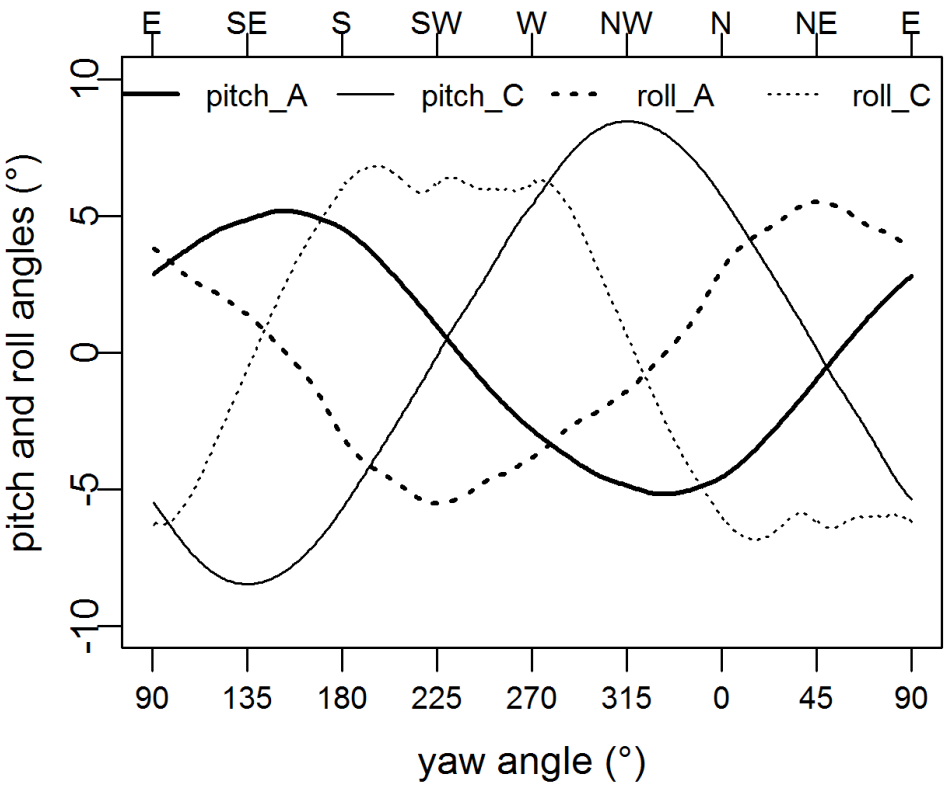

Figure 7: Evolution of the wind-oriented topography (along-wind slope – equivalent to pitch angle – and across wind slope – equivalent to roll angles – on y-axis) with respect to the wind direction (yaw angle as x-axis, 0° is north, 90° is east) for fields A (thick lines) and C (thin lines). The solid lines represent the pitch angles, and the dashed lines represent the roll angles. The slope angles are calculated with a 1° yaw angle step.

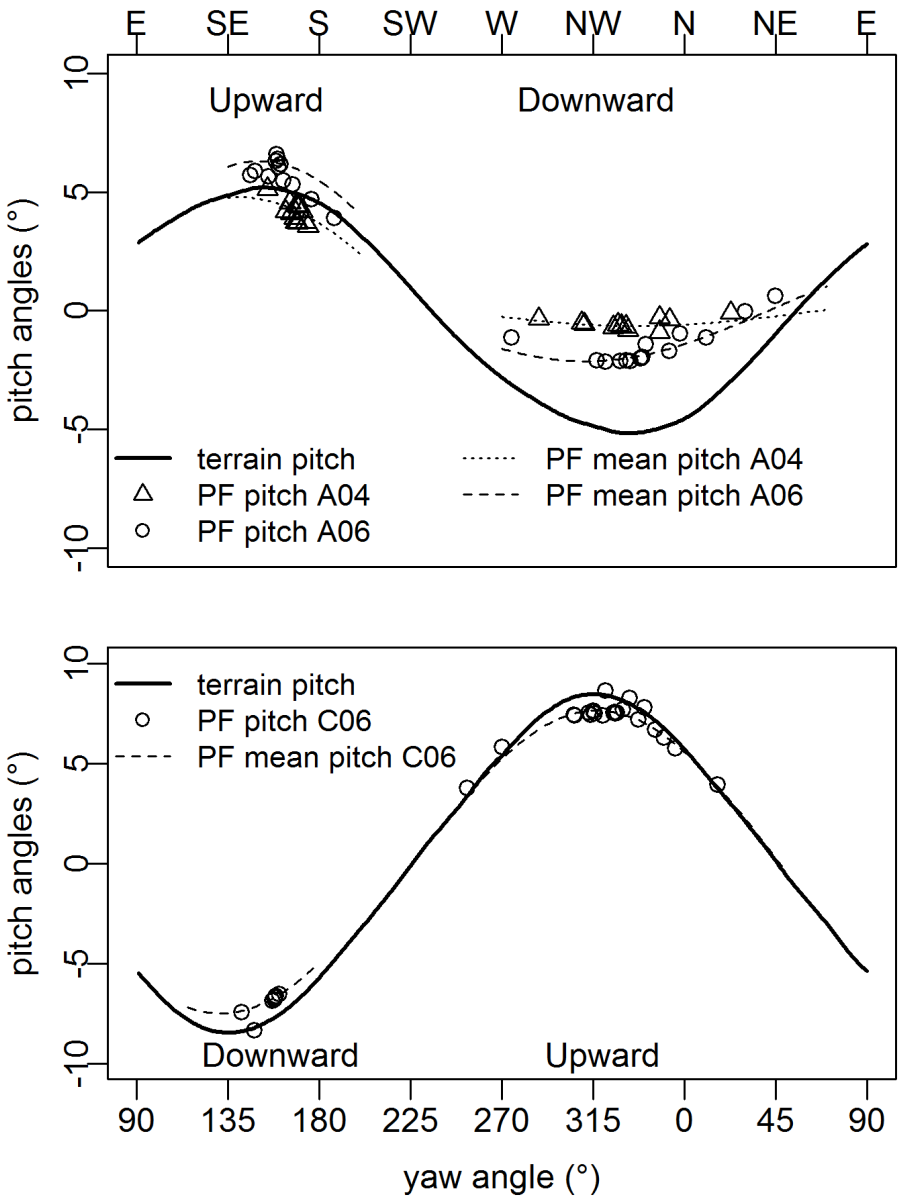

Figure 8a: Compared evolution of the planar fit derived pitch angles and the topographical along-wind slopes (y-axis) with respect to the wind direction (x-axis, 0° is north, 90° is east) for fields A (top) and C (bottom). The continuous curves represent the topographical along-wind slope, as derived from the DEM data (same as Fig. 7). The planar fit-derived pitch angles evaluated over the entire datasets (A04, A06, C06) and for each wind sector (south and northwest) are represented by the portions of discontinuous curves (dotted lines for year 2004, dashed lines for year 2006); they are labelled as the "PF mean pitch". The planar fit-derived pitch angles evaluated for each day and each wind sector are represented by symbols (triangles for the year 2004, circles for the year 2006), where each symbol represents a day or a portion of the day during which the wind direction was within a wind sector; they are labelled as the "PF pitch".

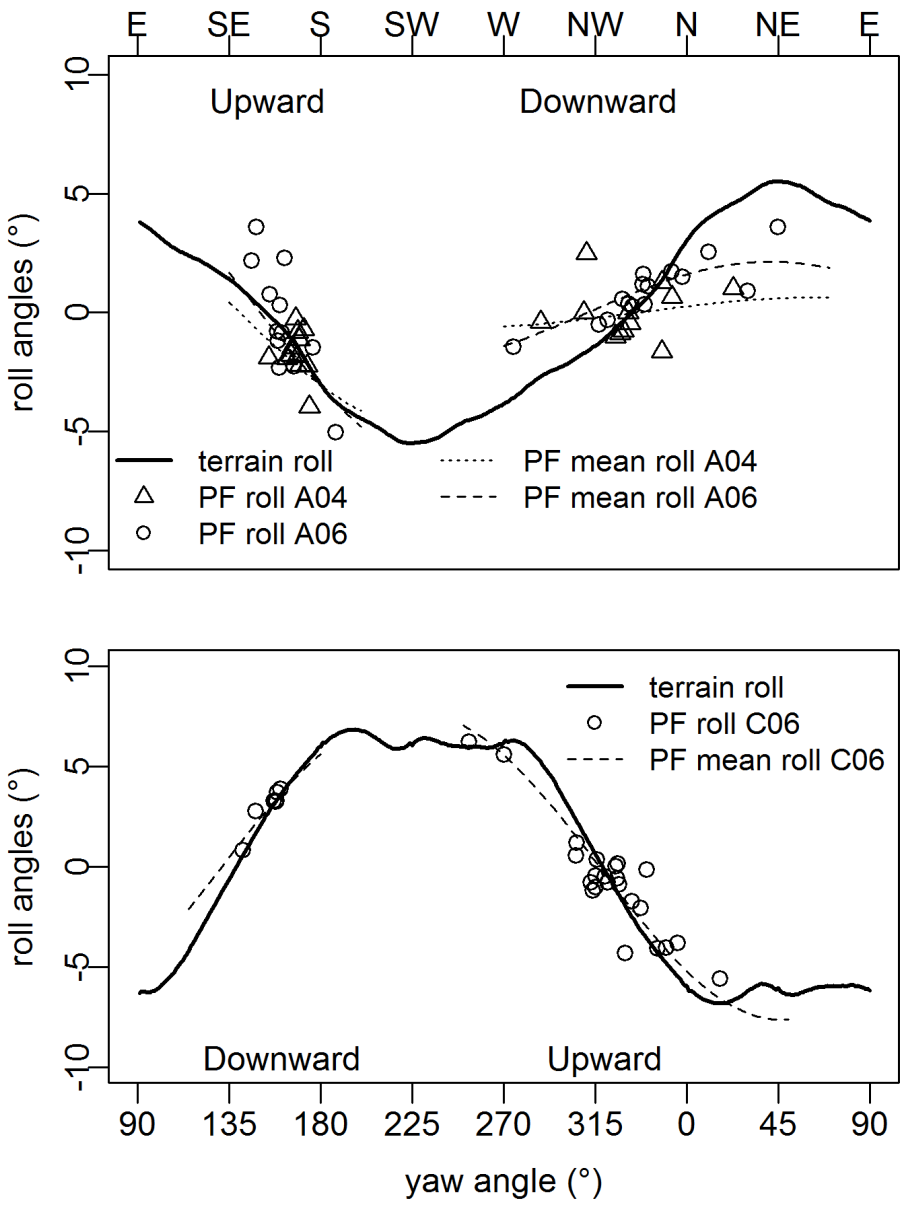

Figure 8b: Compared evolution of the planar fit derived roll angles and topographical cross-wind slopes (y-axis) with respect to the wind direction (x-axis, 0° is north, 90° is east) for fields A (top) and C (bottom). The continuous curves represent the topographical across-wind slope, as derived from the DEM data (same as Fig. 7). The planar fit-derived roll angles evaluated over the entire datasets (A04, A06, C06) and for each wind sector (south and northwest) are represented by the portions of the discontinuous curves (dotted lines for the year 2004, dashed lines for the year 2006); they are labelled as the "PF mean roll". The planar fit-derived roll angles evaluated for each day and each wind sector are represented by symbols (triangles for the year 2004, circles for the year 2006), where each symbol represents a day or a portion of the day during which the wind direction was within a wind sector; they are labelled as the "PF roll".

1206

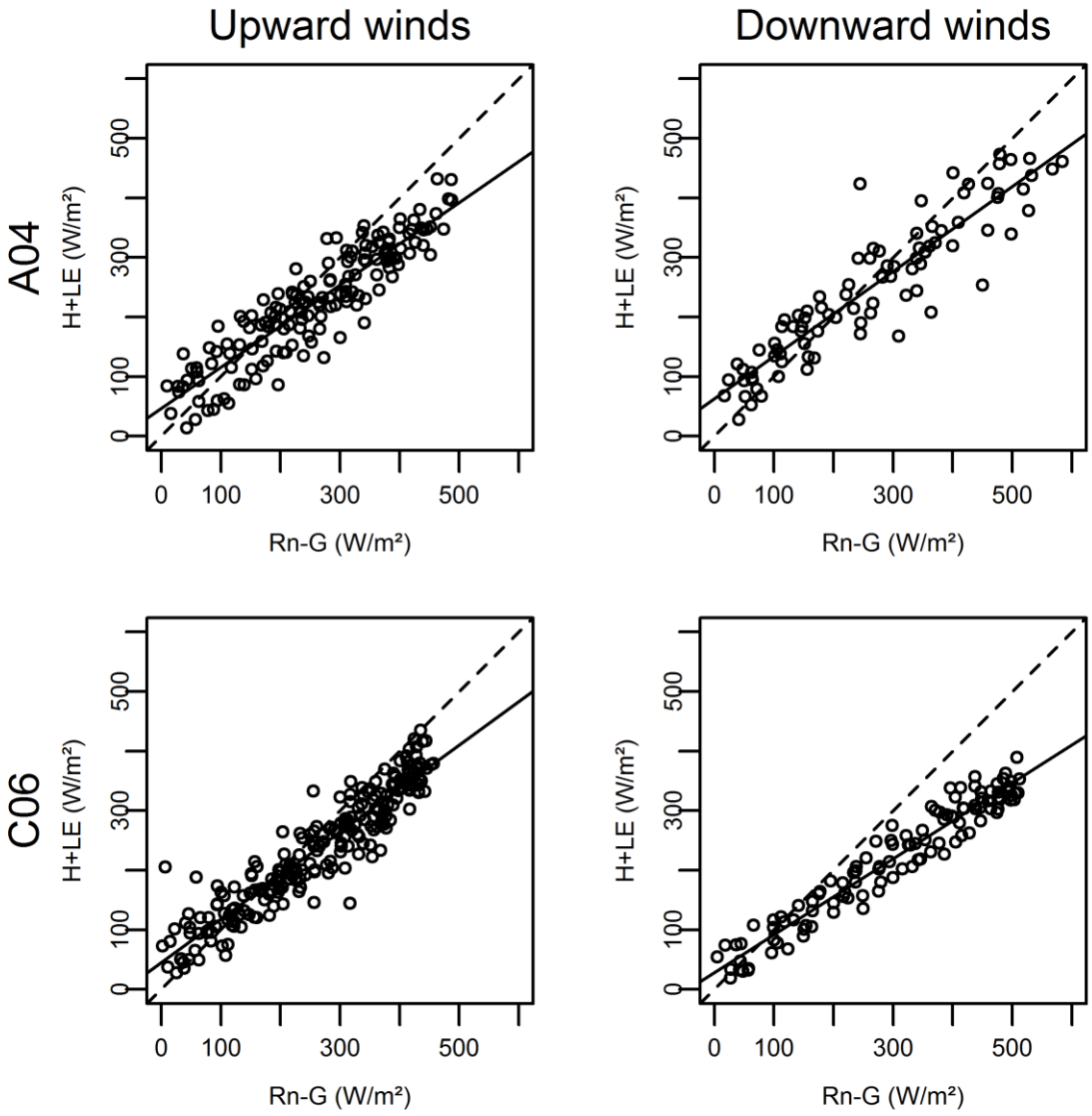

1207
1208
1209 Figure 9: Energy balance closure for the datasets A04 (top line) and C06 (bottom line) and for
1210 the upward winds (left column) and downward winds (right column). The available energy
1211 Rn-G (W m^{-2}) is on the x-axis, and the convective energy H+LE (W m^{-2}) is on the y-axis. The
1212 data correspond to the 30-minute intervals. The dashed line is the 1:1 line, and the continuous
1213 line is the y-axis data versus x-axis data regression line (regression coefficients are given in
1214 Table 3).
1215

1 Table captions

Table 1: Listing of the instruments that were deployed for each flux station in fields A and C for the years 2004 and 2006.

Table 2: Results from the quality control on the turbulent fluxes. The steady-state (ST) test is applied to the friction velocity ($u_* \propto \overline{u'w'}$), sensible heat flux ($H \propto \overline{T'w'}$) and latent heat flux ($\lambda E \propto \overline{q'w'}$). The integral turbulence characteristics (ITC) test compares the flux-variance similarities to those given by the Monin-Obukhov similarity theory. For both the ST and ITC tests, the table gives the proportion of the data belonging to the three quality classes: high quality (ST and ITC values between 0 and 0.3), good quality (ST and ITC values between 0.3 and 1.0) and data not meeting the quality requirements (ST and ITC values greater than 1.0).

Table 3: Statistical indicators for characterising the energy balance closure through the comparison of convective energy (CE = H+λE) as the y-axis variable against the available energy (AE = Rn-G) as the x-axis variables. N is the data number. Terms a and b are, respectively the slope and the intercept of the y = a x+b linear regression (continuous lines on Fig. 9). R^2 is the coefficient of determination between y and x. RMSD is the root mean square difference between y and x. URMSD is the unsystematic RMSD, defined as the scattering around the y = a x+b linear regression. EBR is the energy balance ratio defined as EBR = CE / AE. EB-RES is the energy balance residual, defined as EB-RES = AE - CE. The metrics used here were selected from among those reviewed by Kustas et al. (1996) and Wilson et al. (2002).

1240
1241

Instrument	Field A Year 2004	Field A Year 2006	Field C Year 2006	Frequency of acquisition	Frequency of storage
Data logger	CR23X (Campbell Scientific Inc., USA)				
Sonic anemometer	CSAT3 (Campbell Scientific, USA)		Young-81000V (R.M. Young, USA)	10 Hz	10 Hz
Krypton hygrometer	KH20 (Campbell Scientific, USA)	-	KH20 (Campbell Scientific, USA)	10 Hz	10 Hz
Net radiometer	NR-lite (Kipp & Zonen, The Netherlands)			1s	30 mn
Soil heat flux sensors	Three HFP01 (Hukseflux, The Netherlands)			1s	30 mn
Thermo-hygrometer probe	HMP45C (Vaisala, Finland)			1s	30 mn

1242
1243 Table 1: Listing of the instruments that were deployed for each flux station in fields A and C
1244 for the years 2004 and 2006.
1245
1246

	ST			ITC		
	$\overline{u'w'}$	$\overline{T'w'}$	$\overline{q'w'}$	σ_w/u_*	σ_u/u_*	σ_T/T_*
<0.3	96%	96%	70%	99%	95%	63%
0.3 - 1	3%	2%	16%	1%	4%	34%
>1.0	2%	2%	14%	0%	0%	2%

Table 2: Results from the quality control on the turbulent fluxes. The steady-state (ST) test is applied to the friction velocity ($u_* \propto \overline{u'w'}$), sensible heat flux ($H \propto \overline{T'w'}$) and latent heat flux ($\lambda E \propto \overline{q'w'}$). The integral turbulence characteristics (ITC) test compares the flux-variance similarities to those given by the Monin-Obukhov similarity theory. For both the ST and ITC tests, the table gives the proportion of the data belonging to the three quality classes: high quality (ST and ITC values between 0 and 0.3), good quality (ST and ITC values between 0.3 and 1.0) and data not meeting the quality requirements (ST and ITC values greater than 1.0).

	A04		C06	
	Upward flows	Downward flows	Upward flows	Downward flows
N (-)	155	99	233	120
Slope a (-)	0.69	0.71	0.73	0.64
Intercept b (W m^{-2})	47.0	63.3	44.8	28.2
R^2 (-)	0.82	0.84	0.88	0.93
RMSD (W m^{-2})	63.7	65.5	55.6	100.9
URMSD (W m^{-2})	39.6	47.4	34.9	25.6
EBR (-)	0.87	0.95	0.90	0.73
EB-RES (W m^{-2})	32.7	12.2	26.9	81.2

Table 3: Statistical indicators for characterising the energy balance closure through the comparison of convective energy (CE = H+λE) as the y-axis variable against the available energy (AE = Rn-G) as the x-axis variables. N is the data number. Terms a and b are, respectively the slope and the intercept of the y = a x+b linear regression (continuous lines on Fig. 9). R^2 is the coefficient of determination between y and x. RMSD is the root mean square difference between y and x. URMSD is the unsystematic RMSD, defined as the scattering around the y = a x+b linear regression. EBR is the energy balance ratio defined as EBR = CE / AE. EB-RES is the energy balance residual, defined as EB-RES = AE - CE. The metrics used here were selected from among those reviewed by Kustas et al. (1996) and Wilson et al. (2002).

Figure

Click here to download high resolution image

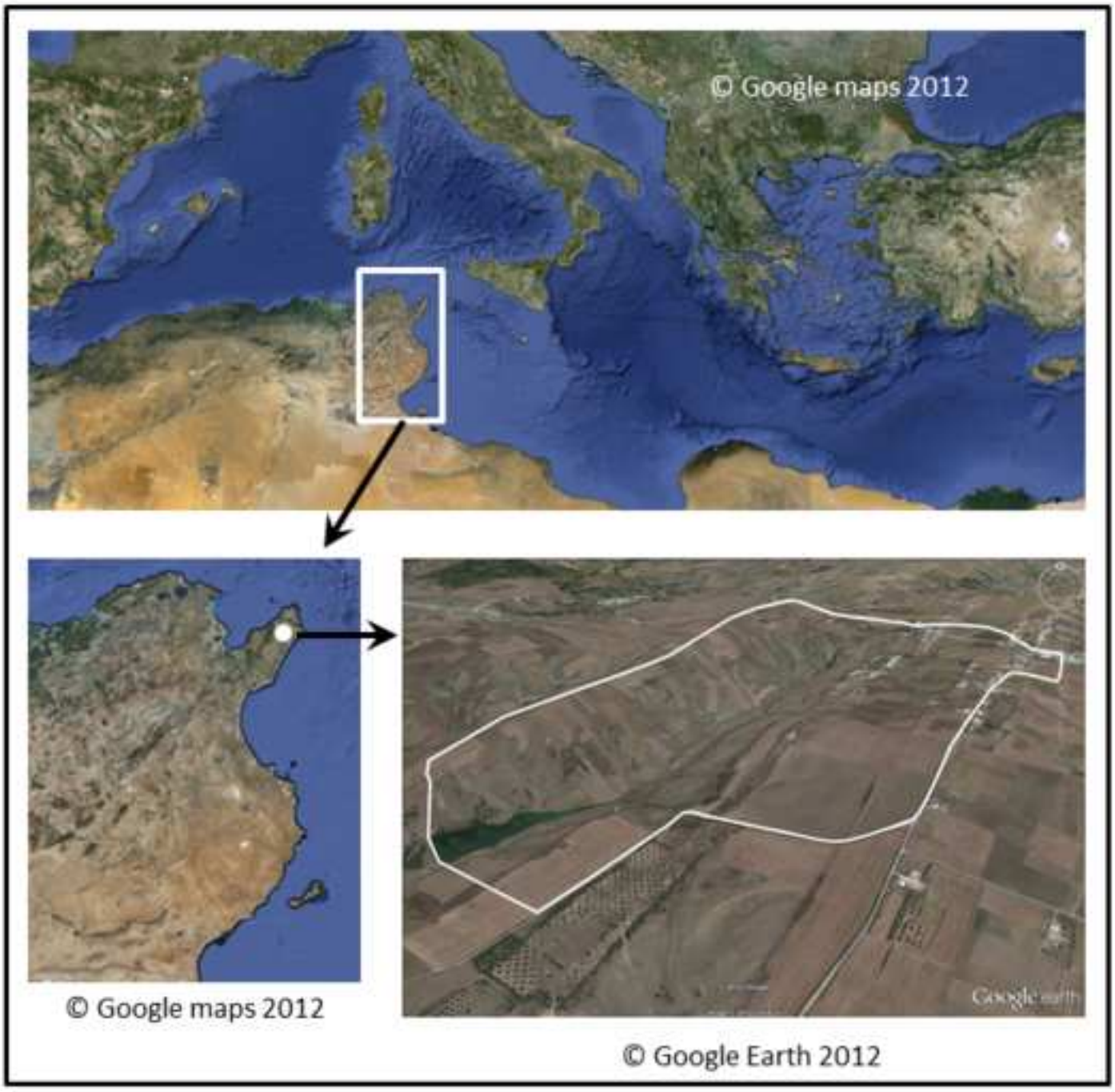

Figure

Click here to download high resolution image

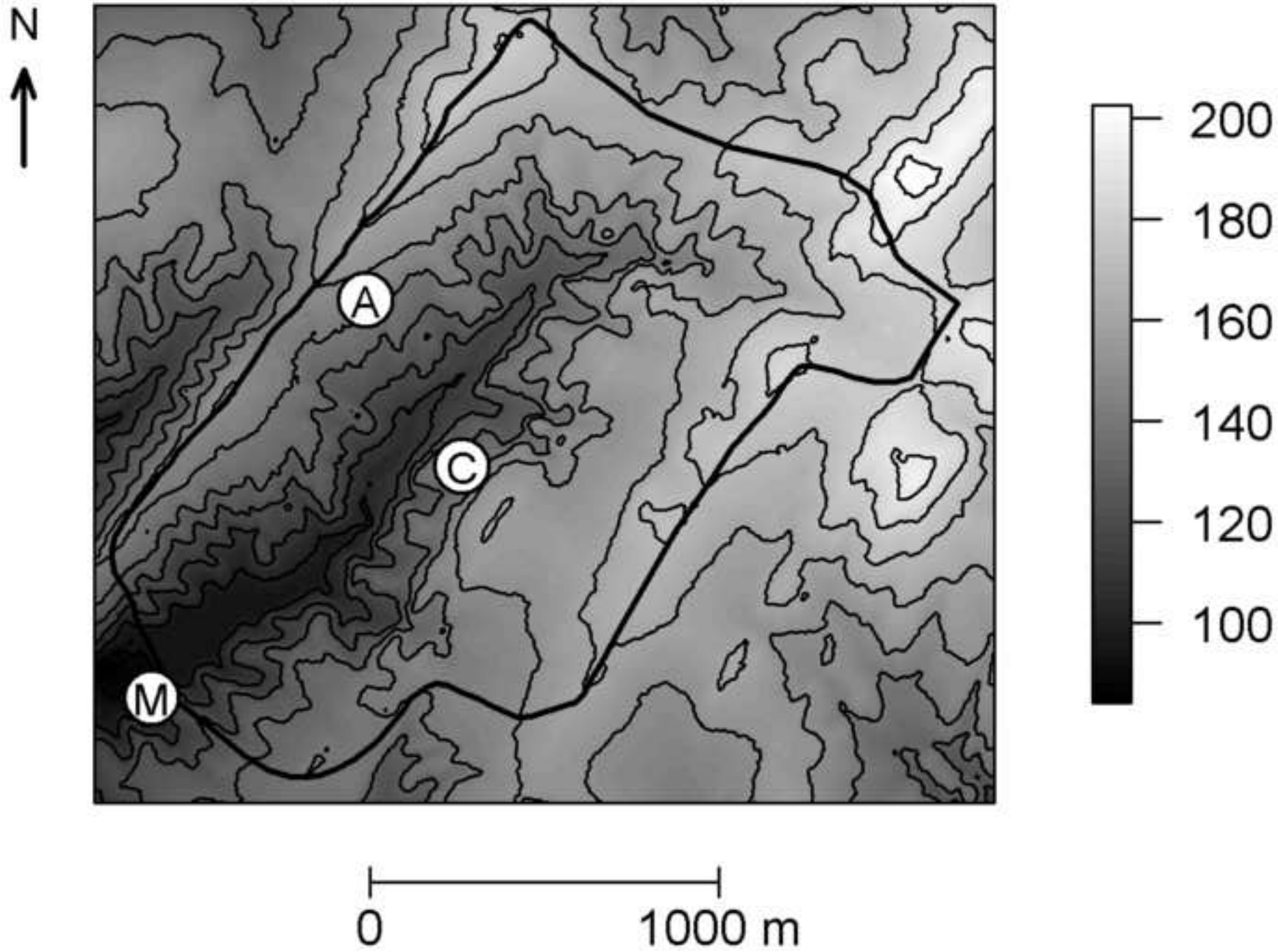

Figure
Click here to download high resolution image

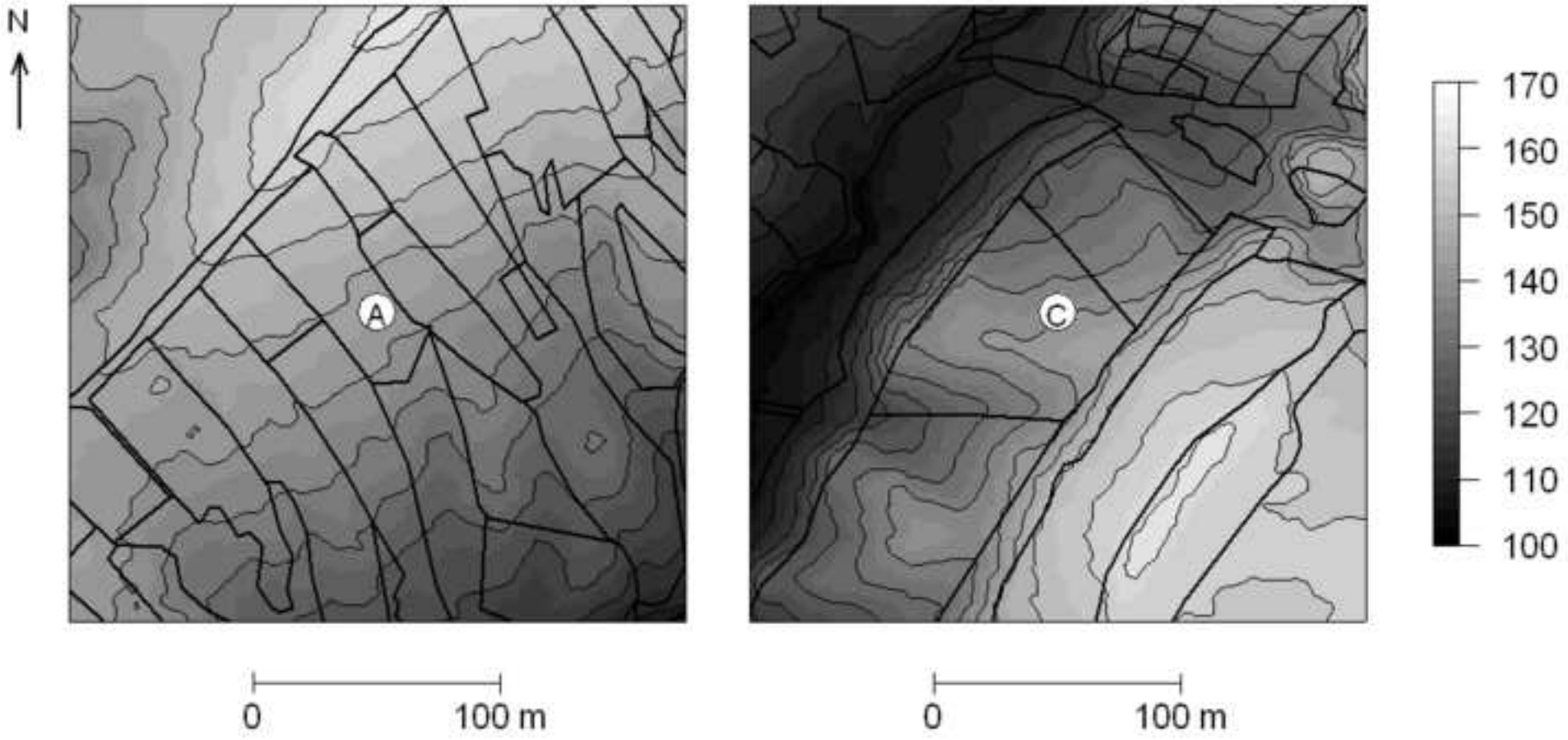

Figure
Click here to download high resolution image

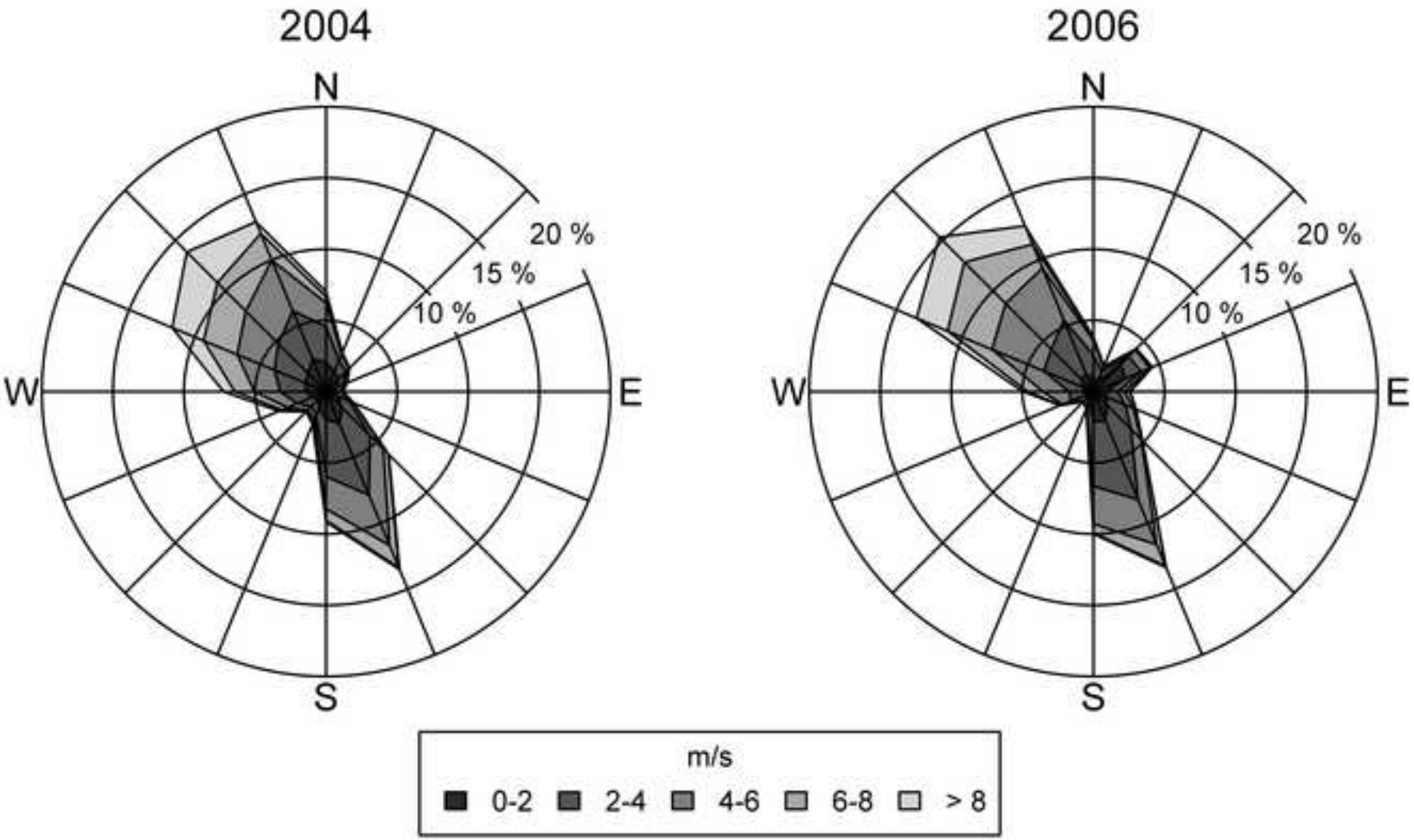

Figure
Click here to download high resolution image

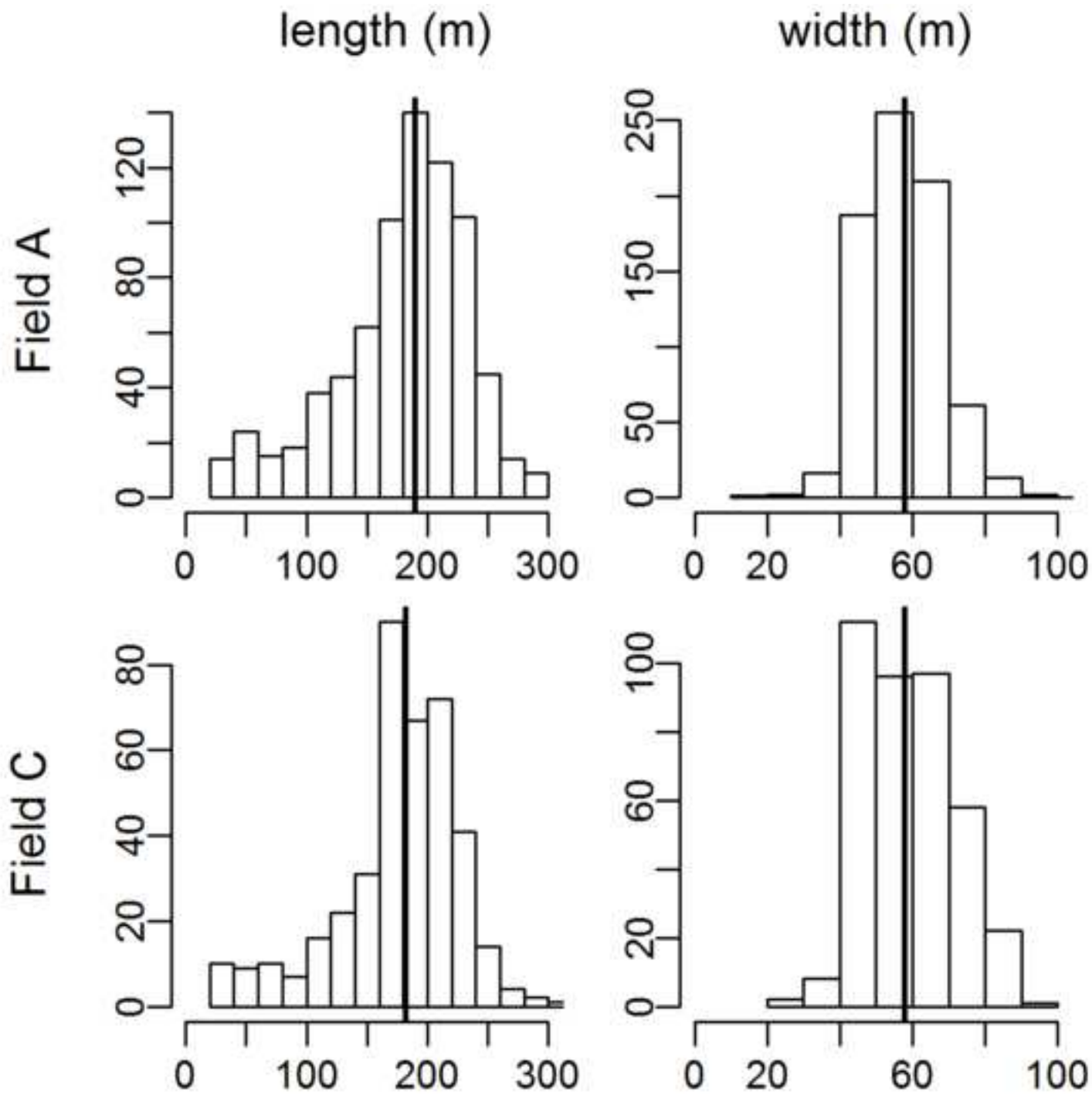

Figure

Click here to download high resolution image

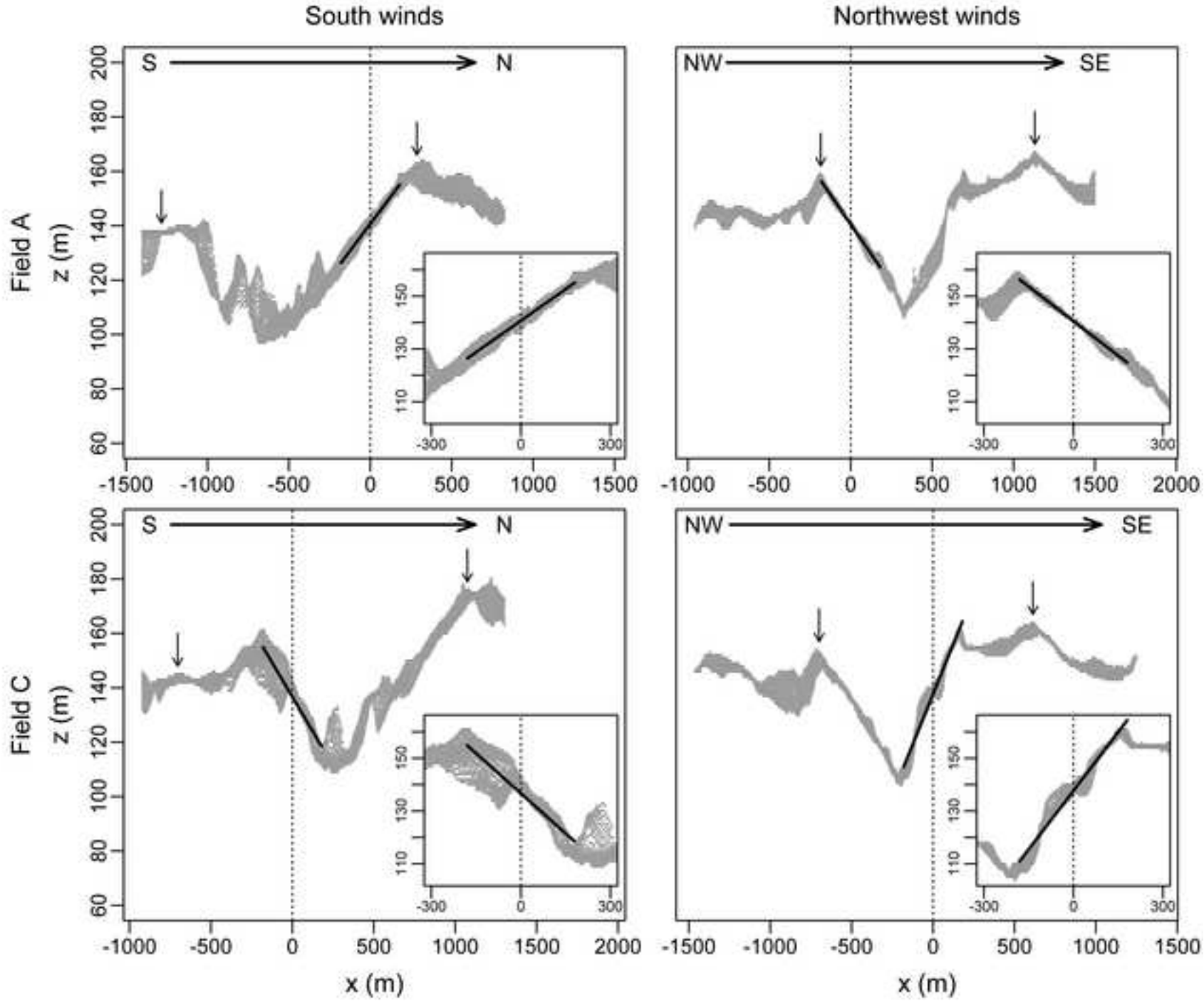

Figure
Click here to download high resolution image

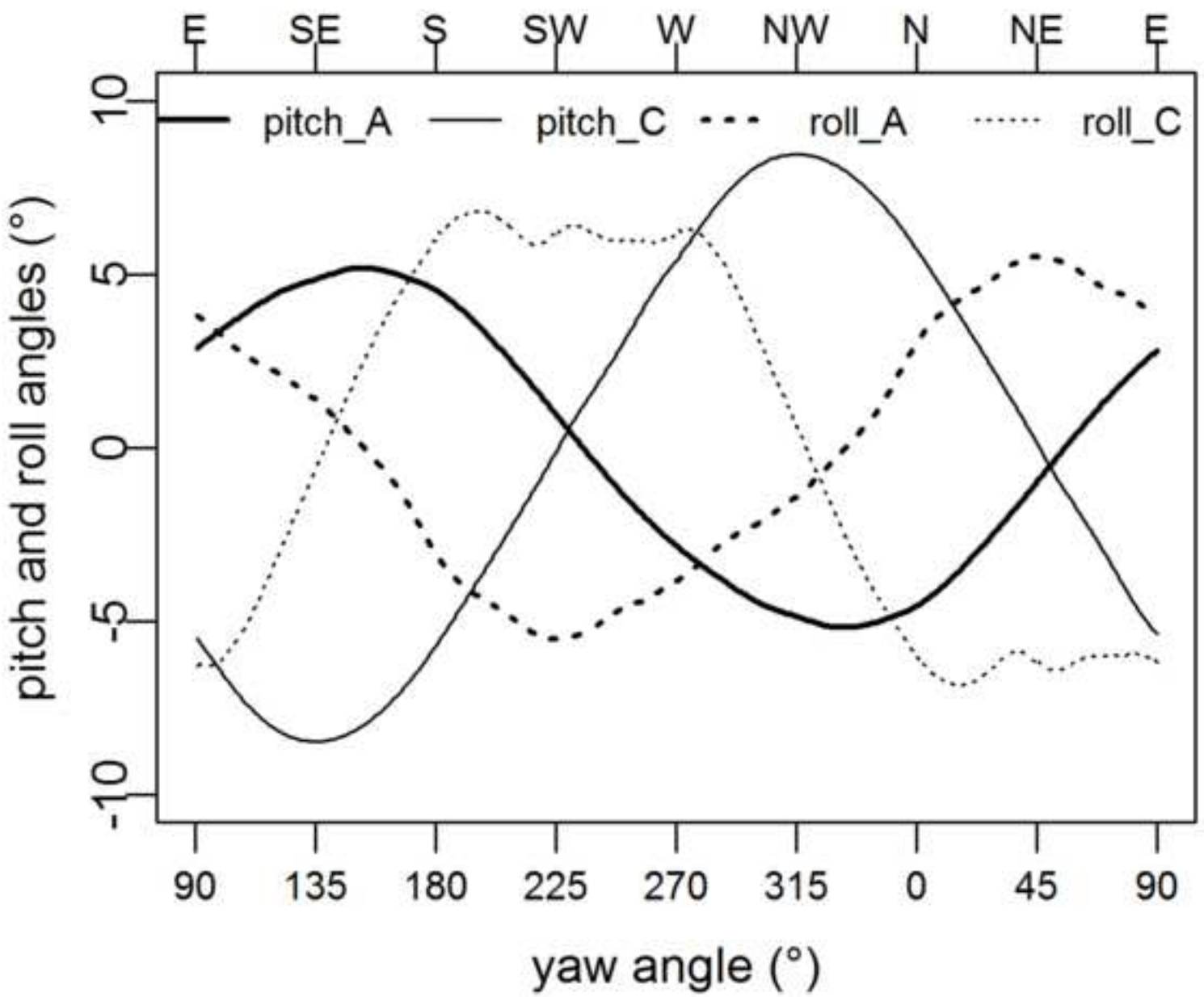

Figure
Click here to download high resolution image

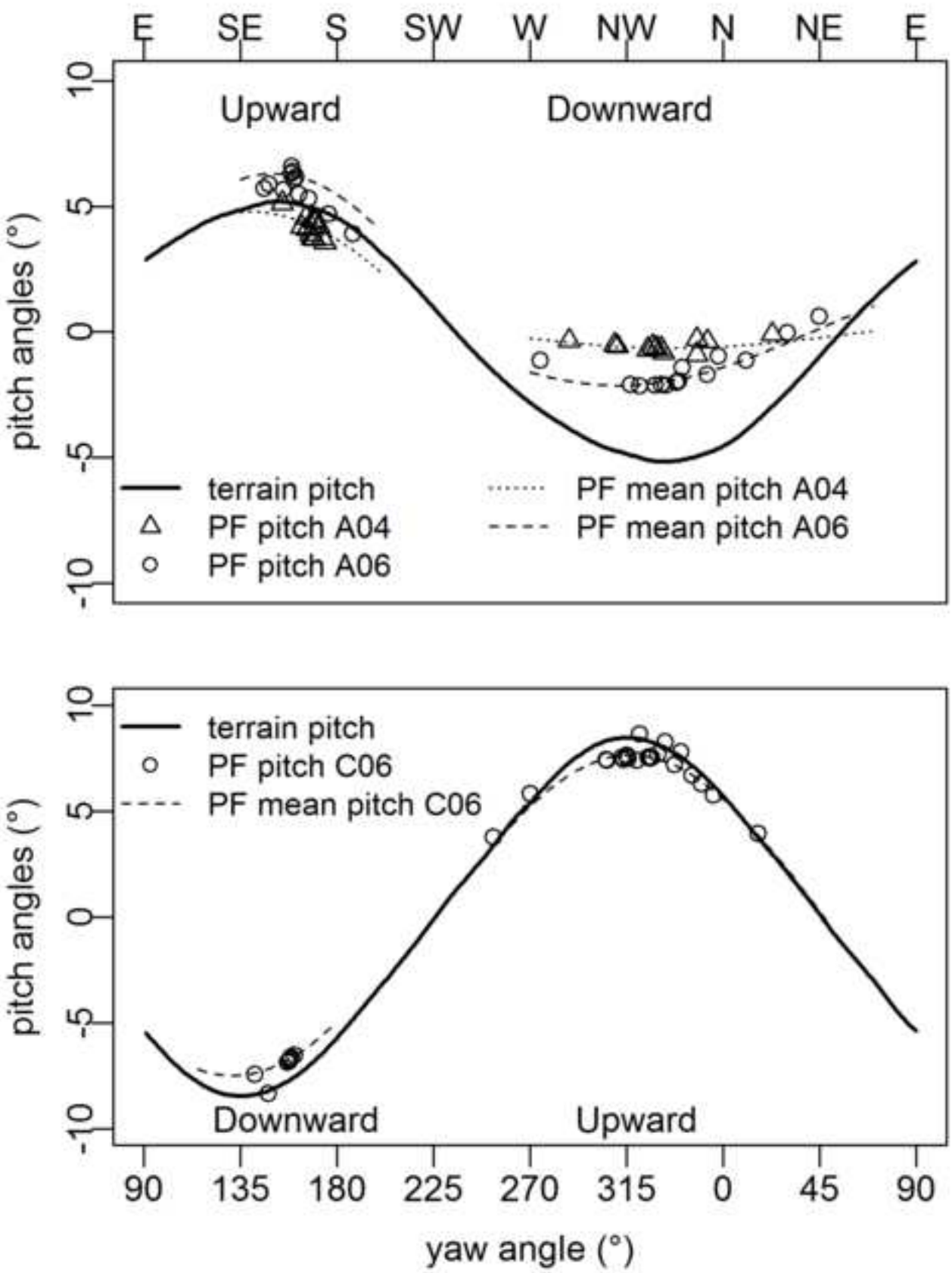

Figure
Click here to download high resolution image

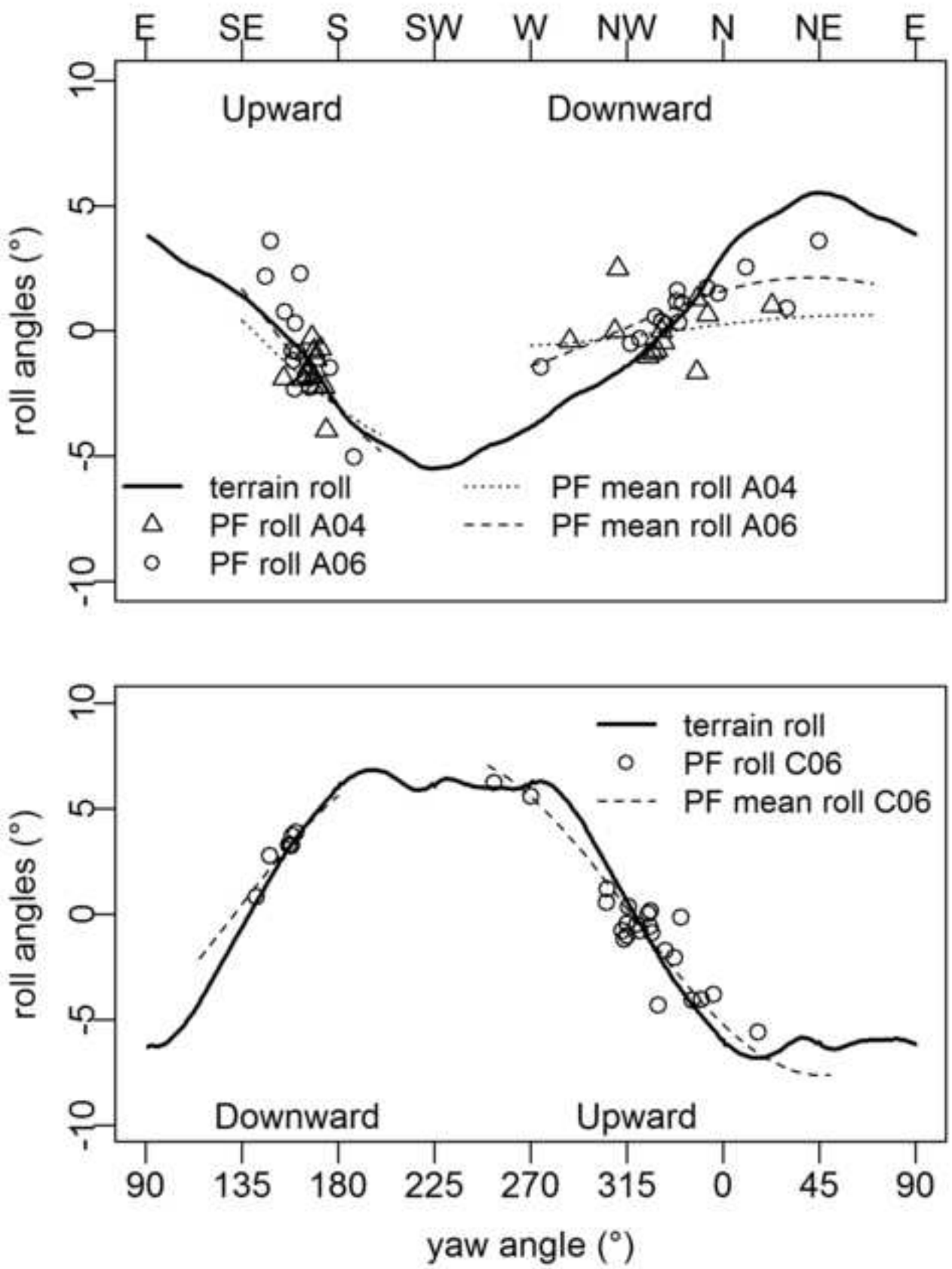

Figure
Click here to download high resolution image